UNIVERSIDAD DE CHILE
FACULTAD DE CIENCIAS FÍSICAS Y MATEMÁTICAS
DEPARTAMENTO DE INGENIERÍA ELÉCTRICA

LED-BASED SUN PHOTOMETER NETWORK FOR DYNAMIC AOD CHARACTERIZATION

TESIS PARA OPTAR AL GRADO DE
MAGÍSTER EN CIENCIAS DE LA INGENIERÍA, MENCIÓN ELÉCTRICA

CRISTÓBAL NICOLÁS GARRIDO CÁCERES

PROFESOR GUÍA:
MARCOS DÍAZ QUEZADA

PROFESOR CO-GUÍA:
ROBERTO RONDANELLI ROJAS

MIEMBROS DE LA COMISIÓN:
MARCOS ORCHARD CONCHA
RICHARD QUEREL

SANTIAGO DE CHILE
2020

LED-BASED SUN PHOTOMETER NETWORK FOR DYNAMIC AOD CHARACTERIZATION

El espesor óptico de los aerosoles (AOD) es la tasa de agotamiento radiativo en la atmósfera causada por estas partículas. Los fotómetros solares y LIDAR son instrumentos para medir AOD, tienen buena resolución y precisión temporal, pero una resolución espacial baja debido a su alto costo. También existen radiómetros en satélites tienen una mejor resolución espacial pero baja precisión y resolución temporal.

Este trabajo busca llenar el vacío entre la resolución espacial y la precisión desarrollando un fotómetro solar automático y de bajo costo para caracterizar la variabilidad de AOD en ciudades, utilizando los instrumentos en red. Se sigue un enfoque iterativo en el diseño, el costo final es de USD 218 por instrumento. Además, se propone una nueva metodología de calibración y se compara con el procedimiento típico, teniéndose resultados similares.

Finalmente, siete unidades midieron AOD durante unos días en Santiago. Las mediciones muestran la variabilidad de aerosoles en la ciudad. Este trabajo presenta el diseño, metodología, calibración y campañas de los instrumentos. La capacidad automática lograda media fue de 15 días de medición continua, la precisión estimada de las mediciones de AOD es inferior a 0,02 y la consistencia en el tiempo es de más de un mes.

Summary

The Aerosol Optical Depth (AOD) is the aerosols' rate of radiative depletion in the atmosphere. Sun Photometers and LIDARs are instruments to measure AOD. They have fair temporal resolution and accuracy but low spatial resolution due to their high cost. Radiometers carried in satellites are also used. They have a better spatial resolution but low accuracy and temporal resolution.

This work aims to fill in the gap on spatial resolution and accuracy by developing an automatic and low-cost Sun Photometer to characterize the AOD variability in the city. The concept is to use those instruments as a network.

An iterative approach in the design and development was followed, achieving a cost of USD 218 per instrument. Moreover, a novel calibration methodology was proposed and compared with the typical procedure. The method proposed in this work had similar results. Finally, seven units measured AOD during some days in Santiago. The measurements show the variability of aerosols in the city.

This work presents instruments' design, methodology, calibration, and campaigns. The automatic capability achieved was a mean of 15 days of continuous measurement, the estimated accuracy of AOD measurements is under 0.02, and the consistency in time is of more than a month.

Sólo el que ensaya lo absurdo es capaz de conquistar lo imposible

Miguel de Unamuno

Acknowledgments

The path from a concept or an idea to a functional product is long and turbulent. It starts from learning how to do the thing, integrates the modules, tests the prototypes to fail and try again, and fail again and again until having something functional. Although the results are right, it does not satisfy the initial expectations. As Winston Churchill said: 'Success consists of going from failure to failure without loss of the enthusiasm'. With that in mind, this work would be summarized as an ode to persist.

Fortunately, the results of this job have overpasses the initial expectations, but not in how we expected. This document exhibit a methodology to design a new device in an agile way, taking advantage of the novel manufacturing technologies to integrate a mechanical, electronic, and software design in a functional product. Moreover, the cost of development has been reduced, considering this methodology only adds the tiniest elements to satisfy the requirements. This learning could be extended to many other areas that require technological disruptions and to address some of the most severe challenges for the future.

During the network implementation, several locations were required to install the instruments. Thanks to Professor Marcos Díaz and his family for allowing La Reina, Maipú and Gran Avenida stations' measurements, Professor Roberto Rondanelli helped with logistics with the Geophysical Department. Thanks to José Miguel Campillo and Patricio Mella from the Department of Geophysics of the University of Chile, who helped me install some prototypes. Thanks to Professor Nicolás Hunneus, his family, and Mr. Luis Merchant for allowing the Malloco station's installation. Also, thanks to the Science Faculty of the University for letting us install the Ciencias station, Professor Jorge Silva for Pudahuel station, Professor César Fuentes for helping us with Cerro Calán station, my family for La Florida Station, and to the owners of the house in Padre Hurtado whose I have not the opportunity to meet. I apologize If I forgot someone, but feel free included it in this extensive list.

Last but not least, I must acknowledge the vital contribution to enrich this work to Professors Marcos Díaz, Marcos Orchard, Roberto Rondanelli, and Dr. Richard Querel. They patiently corrected this document and helped to obtain a better version of it.

Contents

List of Tables

List of Figures

Chapter 1

Introduction

Atmospheric aerosols are small particles suspended in the atmosphere with a lifetime on the order of days or a few weeks. Aerosols impact the earth's surface radiation budget, clouds formation serving as Cloud Condensation Nuclei (CCN), and human health [1]. The dynamic of aerosols and their impact on the weather can be measured and analyzed using the Aerosol Optical Depth (AOD).

The AOD is the rate of depletion (in logarithmic scale) of monochromatic radiance caused by aerosols in an airmass column, according to Beer-Lambert-Bouguer's Law. AOD is related to the number of particles present in the column [2] and the particle size distribution. The distribution of the particle sizes can be estimated using the Ångström exponent [3]. This distribution is essential to understand clouds formation, rains and ascertain the possible origin of the particles. AOD measurements for different wavelengths are needed to calculate the Ångström exponent.

The instruments to measure AOD may be characterized by the quality of their temporal resolution, spatial resolution, and accuracy. The currently available devices include ground-based Sun Photometers and LIDARS. Additionally, satellite radiometers or LIDARs with retrieval algorithms (e.g., MODIS, CALIOP) are used to estimate AOD as one of their satellite products.

Sun Photometers have a low spatial resolution when working in networks (e.g., AErosol RObotic NETwork (AERONET) [4], where each point of measurement represents a large area, such as a City)). On the other hand, they have fair temporal resolution and accuracy. They are considered the ground truth instruments to measure AOD. In the case of satellite products, they cover large areas per measure. However, they have a relatively low temporal resolution, and accuracy [5]. Some new satellite products might have a higher temporal resolution, such as from GOES, for instance.

Holben et al. (2018) support the need for higher spatial resolution with ground-based instrument measurements. AERONET Sun Photometers could be an option because they have an excellent AOD accuracy of 0.01 or less depending on the wavelength (in their latest versions). However, the instruments are hundreds or thousands of kilometers apart from

each other. Satellite measurements, such as those taken by MODIS and CALIOP, have a worse accuracy than AERONET Instruments [5], especially for low values of AOD, how they could be found in Santiago de Chile. Therefore, there are not measurements that satisfy the three characteristics of accuracy, temporal, and spatial resolution with current approaches and instruments.

There are particular campaigns called Distributed Regional Aerosol Gridded Observation Networks (DRAGON) that use several AERONET Sun Photometers in a high-density area (they use among 6 and 43 instruments). However, the temporal resolution only considers a few months of measurements [6]. Furthermore, to make a high-density Sun Photometer Network, the DRAGON campaign's approach requires some realizable conditions. For example, Chile has only a few AERONET Sun Photometers (less than 10 for the whole country). Therefore, a campaign such as DRAGON would imply the acquisition and installation of several instruments. That means a DRAGON campaign is not feasible at this moment considering the economic and logistic costs.

Satellite measurements and products have two main weaknesses. They have poor accuracy for low and medium AOD values. For example, typical maximum values at 500 nm for Santiago de Chile are around 0.8 and 1.0, which is low compared with some places in Asia. Typical reported Root Mean Square Error (RMSE) of satellite products respecting AERONET are 0.12 in the case of MODIS (two wavelengths) [7] and between 0.09 and 0.05 (3 wavelengths) for GOES-16 products [8]. Moreover, low orbit satellites can only take two measures per day at the same place. Instruments mounted in geostationary satellites have been solving the last problem. Given these disadvantages, satellite measurements cannot take adequate measurements of AOD with a high spatial resolution..

Because of the limitations of temporal and spatial resolution, and accuracy, other instruments are required to take aerosol measurements. Toledo et al. (2018) describe a low-cost and hand-held Sun Photometer based on the GLOBE Sun Photometer [9]. These instruments have better accuracy than satellite AOD measurements using the AERONET Sun Photometer as ground-truth. Furthermore, they have been able to obtain distributed measurement results at the city scale network. In contrast, hand-held instruments create logistic problems. They are not feasible for long-term campaigns of a high-density Sun Photometer network. Handheld Sun Photometer networks allow measurements of fair spatial resolution and accuracy. However, automatic instruments are necessary to improve temporal resolution.

Consequently, the present work describes the development of an Inexpensive Automatic Sun Photometer, an improved version based on the Toledo et al. [10] instrument. This instrument can work autonomously. It was designed to reach a city-scale network, with fair temporal and spatial resolution and accuracy.

An iterative approach is used to design and develop the prototype instrument. In addition, a new calibration procedure is proposed and evaluated. After that, several units of the prototype are built, and a city-scale campaign is performed. Finally, the obtained results are studied; the results and issues are registered with the improvements for future versions.

This work's main objective is to determine the feasibility of implementing a low-cost, automatic city-scale Sun Photometer Network to study the AOD variability. The metrics to

evaluate the instrument are their cost of materials, the error of the measurements respect the ground truth instrument and among the prototype units, and the variability of the measurements in distributed campaigns.

To this end, the first objective was to develop, calibrate, and characterize an instrument prototype. Then, to manufacture several units and to perform some distributed campaigns at the city-scale. The last objective is to identify the issues, recommendations, and requirements for the future implementation of a network. In this work, the methodology used to make the prototypes is presented, characterized them, and the results and findings of our city-scale measuring campaigns.

1.1. Content of this document

Chapter 2 summarizes state of the art in the field is summarized. Chapter 3 presents the background needed to understand how the AOD is measured. Chapter 4 shows the differences in our automated version concerning the Toledo et al. (2018) Sun Photometer. Chapter 5 compares the calibration methodology proposed in the methodology section and study all our instruments' consistency. Next, we present AOD measurements for some days of our prototype network. Chapter 6 discusses the results and proposes some improvements or critical points to consider in the future developing of a high-density Sun Photometer network. Finally, the main conclusions and future possibilities of this work are established. In the following, the central hypothesis and objectives are summarized.

1.2. Hypothesis of this Work

A low-cost Sun photometer network composed of automatic instruments can characterize the aerosols variability in urban areas. Therefore, if these instruments are developed and tested under real conditions, it will be possible to observe this behavior in the aerosols.

1.3. Main Objective

To determinate the feasibility of implementing a low-cost, automatic city-scale Sun Photometer Network. The metrics to check this objective are the cost of the material per device, the achieved error in the measurements compared with other instruments and themselves, and the distributed measurements of AOD in the city.

1.4. Specific Objectives

1. To develop, to calibrate, and to characterize an instrument prototype. The instrument must track the Sun with enough accuracy to measure with an error between the AERONET Sun Photometers and the Satellite products. Furthermore, a calibration process must be proposed and validated to determine the value of the measurements. Finally, the instrument measurements must be compared with the ground truth. The Root Mean Square Error (RMSE) between the prototype and the AERONET Sun pho-

tometer measurements is the first quantitative metric to evaluate the achievement of this objective.

2. To manufacture several units and to perform some distributed campaigns at the city-scale. The measurement variability among all the units must be compared using the standard deviation. Finally, the on-field distributed measurements are used to determine the variability of aerosols in the city.

3. To summarize the issues found in this work. Furthermore, to establish the requirements to enhance the capabilities of future instruments considering a complete operational Sun photometer network. For example, improvements in the calibration process to reduce the error of the measurements or add other related measurements such as the particle size parameters, or others.

Chapter 2

State of the Art

The efforts to measure the AOD could be divided into two groups of instruments: The ground instruments, separated into autonomous and handheld instruments, and satellite products. There is a trade-off between the accuracy of the measurements and the spatial resolution and between the temporal resolution and the spatial resolution. While the autonomous ground instruments have excellent accuracy and temporal resolution with measurements all day, satellite products only have a few measures during the day for the same place, but covering large areas of the earth.

The current availability of instruments makes it unfeasible to study the variability of AOD in different places of the city for a whole day. In the case of Santiago de Chile, to have this information could be important to determine the sources and sinks of aerosols and the paths that they follow through the city.

To solve those challenges, two different approaches must be considered: the use of geostationary satellites, such as GOES-16, to increase the temporal resolution of satellite products. However, the accuracy is still poor compared with the AERONET Sun Photometers (0.05-0.09 for the GOES-16 products [8] against 0.01 - 0.02 for the AERONET Sun Photometer [4]). The other approach is to use ground instruments as a network. In this case, both automated and manual devices show different issues in their implementation. On one side, manual instruments allow campaigns with several measurement points, but for a short time (some days or some hours for several days) due to the extensive use of people to perform the measurements. On the other side, automated instruments are too expensive and make it difficult to maintain a network of instruments working for a long time. The aim is to develop an automatic and inexpensive Sun Photometer to combine the benefits of both kinds of ground instruments. Take measurements for a long time with an affordable cost of implementation.

The first handheld Sun Photometer was presented by Volz in 1959 [11]. Nowadays, the ground truth in Sun Photometers is the AERONET Network Sun Photometer [4]. This network uses the Cimel Sun Photometer. Another automatic high-performance instrument to measure AOD is the PREDE POM 01 sky-radiometer [12]. Other devices are handheld Sun Photometers instruments. The principal examples are the Microtops Sun Photometer and SIMBAD. All the procedures for these instruments were summarized in [13]. These

instruments were considered under the Sensor Intercomparison and Merger for Biological and Interdisciplinary Oceanic Studies (SIMBIOS) Program published in 2001. The Cimel Sun photometer gives the ground truth accuracy with and standard deviation lower than 0.02 for wavelength under 440 nm and 0.01 for higher wavelengths.

There are cheaper versions of handheld Sun photometers, which use LEDs as photodiodes to measure AOD. Brooks et al. (2001) developed the first LED-based Sun Photometer for the Global Learning Observation to Benefit the Environment (GLOBE) program, and it is the base for all the following developments. Improved versions of this instrument are the Calitoo, and the Toledo et al. (2018) [10] Sun Photometer. Furthermore, there are some automatic versions based on the GLOBE Sun Photometer. Perri et al. (2016) added a Sun tracker to the GLOBE Sun Photometer to demonstrate the feasibility of an automated instrument [14] . Moreover, miniSASP [15] is an independent version of an automated Sun Photometer to use in an Unmanned Automatic Vehicle (UAV). Both versions left the low-cost approach adding capabilities or complexities to the original idea in their developments. A last handheld Sun photometer is presented in [16]. In this case, the instrument is mixed with a Particle Matter Sensor (PM).

Although several articles discuss the uncertainties of this kind of instrument due to the gas effect and the availability of several units, a common value for the mean error is under 0.02. In addition, the handheld instruments cost around USD 100 and USD 200, while automatic instruments cost of materials is in the order of thousands of dollars.

Respecting the network measurements, De Almeida et al. (2007) used several Microtops handheld Sun Photometers to perform the MILAGRO (Megacity Initiative: Local and Global Research Observations [17]) Campaign during 2006 in Mexico City. Moreover, they present that satellite measurements overestimate AOD in urban areas. With a similar approach, Boersma et al. (2006) used several GLOBE Sun Photometers to validate Satellite observations over the Netherlands [18]. Another example of network measurements is the demonstration performed by Toledo et al. (2018). They used their own made instruments to measure in Santiago de Chile during 2016 to show the variability of Aerosols in urban areas during a whole day, in contrast to others that only measured for some hours to compare whit satellite measurements [10]. Ford et al. (2019) perform a pilot city-scale campaign with the instruments presented by Weld et al. (2019) [16, 19]. Finally, NASA has promoted Network campaigns on a regional scale using Cimel Sun Photometers, the DRAGON campaigns [6].

Currently, there are several pieces of research related to the calibration process of high-performance instruments ([12, 20]) and comparison among instruments ([5, 10, 17]). In addition, Toledo et al. (2018) studies the effect of using wide sensors to measure AOD instead of the narrow sensors used by the high-performance instruments. They showed no significant difference between a wide and a narrow band sensor if there are no reactive gases effect in the spectral band of the measurements. However, when those gases are present, Toledo et al. (2018) exhibits a procedure to correct the measurements, knowing the quantity of gas and the spectral response of the sensor by using simulations.

The most recent works [10, 16] exhibit the need to develop an automated version of their Sun Photometers to avoid logistic problems and escalate the number of possible measurements. This work addresses the challenge of proposing the first approach to develop and

operate a city-scale Sun Photometer Network. It has never performed a network campaign with low-cost automatic Sun Photometers. Furthermore, to create the automatic Sun Photometer, the know-how developed by Toledo et al. (2018) is used to propose improvements to the instrument and the calibrations procedures considering the new setup. With this contribution, it could be possible to explore the dynamic behavior of aerosols and improve the AOD estimation of satellites to urban areas.

Another use of aerosols is the retrieval of the particle size distribution. To retrieve the particle size distribution is necessary to measure the AOD for several wavelength channels and estimate the Ångström exponent. [2, 3, 21] present some examples of that. Although the prototype does not allow us to estimate the Ångström exponent, the requirements to do that in future versions are discussed.

Chapter 3

Background

The present section exhibits an overview of aerosols, radiation in the atmosphere, and typical measurement processes. In the first part, it is defined what aerosols are and why their study is essential. It is also shown some concepts related to radiation and its interaction with the atmosphere to determine the Atmospheric Optical Depth (AOD). Finally, the main instruments used to measure AOD are presented.

3.1. Aerosols

The atmospheric aerosols are defined as all the solid and liquid particles in suspension in the atmosphere, i.e., particles with a negligible terminal fall speed [22]. The range of particle size is mainly from 0.01 to 100 μm [23]. Examples of aerosols are dust, combustion result particles, pollen, and others.

Aerosols can be of biological, solid earth, anthropogenic and in-situ-formation origin:

- The biological sources of aerosols include all the particles released in the atmosphere from animals and plants. For example, pollen, seeds, and animal or plant parts. Furthermore, there are natural sources of aerosols, such as oceans that released particles into the atmosphere (people coughing).

- The solid earth sources include particles of dust released by the wind in semiarid soils and deserts.

- The anthropogenic sources are all the human activities that generate aerosols. Examples of that are fossil fuel combustion, the dust of the roads, biomass burning, and other.

Aerosols injected into the atmosphere are called primary aerosols. Moreover, aerosols can react in the atmosphere or collide to create different particles. The aerosols result of reactions, deposition, or collisions in the atmosphere are known as in-situ-formation aerosols, also called secondary aerosols.

The most common continental aerosols are sulfates and ammonium, while the marine

aerosols are Na, Cl, Mg, K, Ca ions. Other typical aerosols are organic aerosols abundant in urban areas.

Wind can transport the aerosols. This transport can reach intercontinental or global scales. For example, small particles of Saharan dust are transported to America and work as Cloud Condensation Nuclei (CCN), contributing to Hurricanes formation. In this work, we are interested in aerosols transport at the city scale.

Once aerosols are released into the atmosphere, they can interact among them. Furthermore, the aerosols are removed from the atmosphere by dry deposition or condensation of water drops. The insertion and removal of Aerosols define the size distribution of aerosols in the atmosphere. Figures 3.1 and 3.2 summarizes the processes and particle distribution of aerosols in the atmosphere.
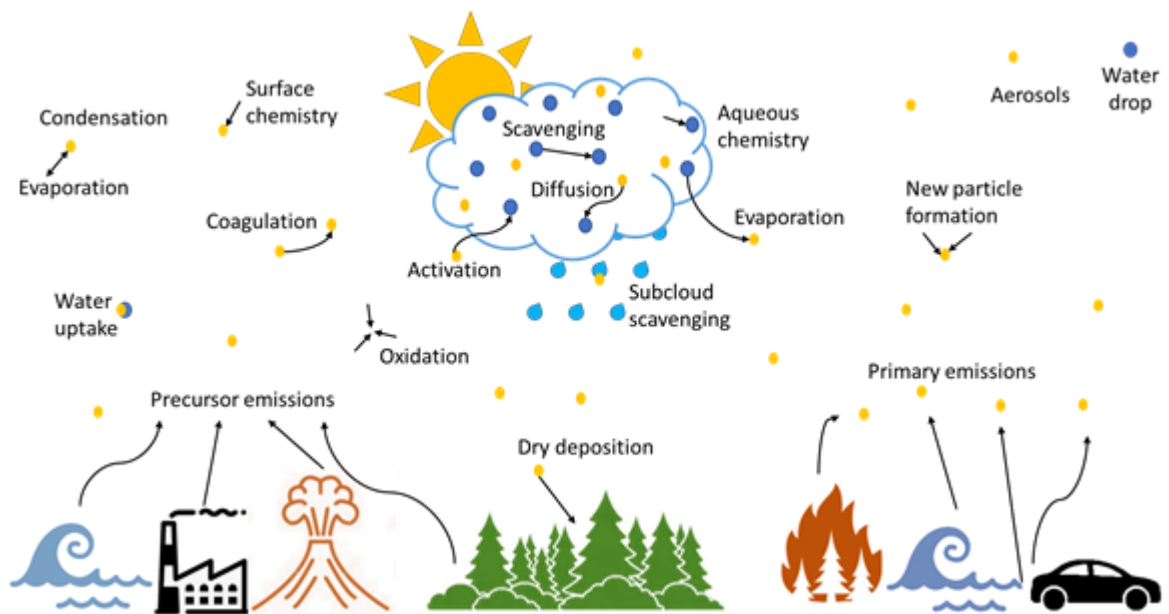
Figure 3.1: Aerosols processes in the atmosphere (adapted from Ghan et al.(2007))

Figure 3.2 displays that the aerosol distribution has three modes: Aitken Nuclei Range $(0 - 0.1 \ \mu\text{m})$, accumulation mode $(0.1 - 1 \ \mu\text{m})$ and the Coarse mode. The first two modes can be grouped in Fine mode. The latter is related to the predominant particle size and the AOD through the so-called Ångström Exponent. Moreover, Figure 3.1 presents the different processes and sources of aerosols in the atmosphere. In essence, aerosols could be introduced in the atmosphere by several sources, and they also could interact with other particles, radiation, and air molecules, changing their chemical composition and size.

3.2. Radiation in the Atmosphere

This section aims to summarize the main concepts of solar radiation and its effects on the atmosphere. It is assumed that the reader has some knowledge of electromagnetic waves, presenting only some concepts and definitions. In the first part of this section, the variables involved in the radiation model are defined, such as scattering and abortion. In the last part
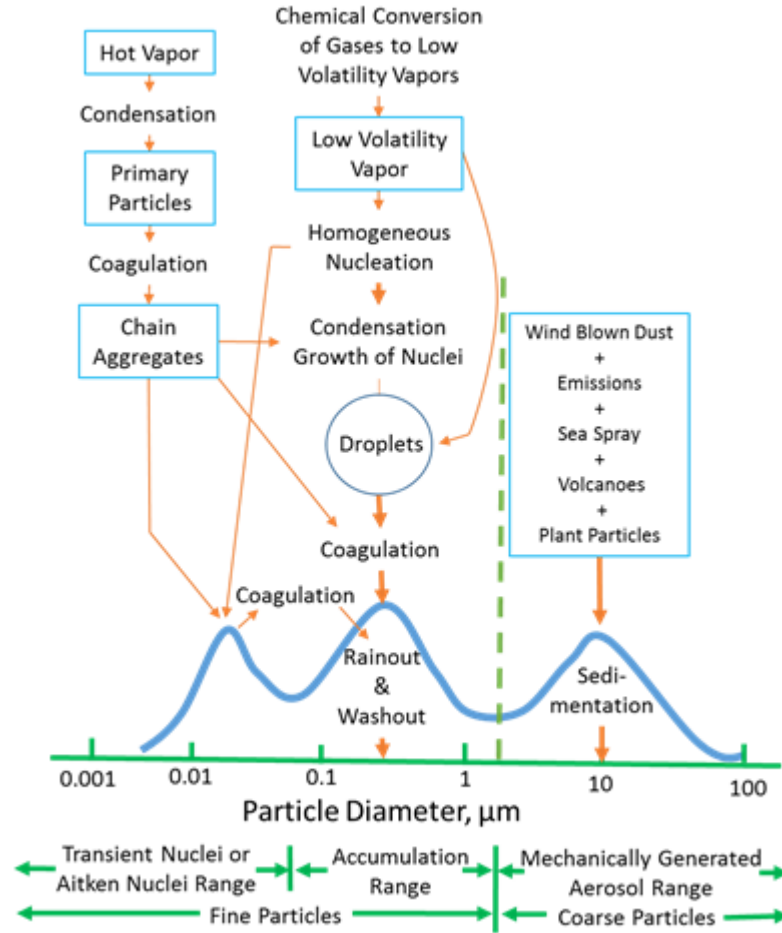
Figure 3.2: Aerosols formation and particle size distribution (adapted from Seinfield et al. (2016))

of the section, the Beer-Lambert-Bouguer's law and the atmospheric optical depth (AOD) definition are presented.

3.2.1.   The Electromagnetic Spectrum

The Sun emits electromagnetic waves at different wavelengths (and frequencies). The electromagnetic spectrum is divided into several parts, depending on their use or characteristics. The Figure 3.3 bellow exhibits some of those divisions. In this work, it is used mostly as the visible part of the electromagnetic spectrum.

In atmospheric sciences, the spectrum is described as respect the wavelength, while in other areas, the description is preferred to respect the wave frequency. In addition to that, in the thesis, the wavenumber is defined as follows:

$$\nu = \frac{1}{\lambda} \tag{3.1}$$

Where ν is the wavenumber, and λ is the wavelength. The units of the wavelength are
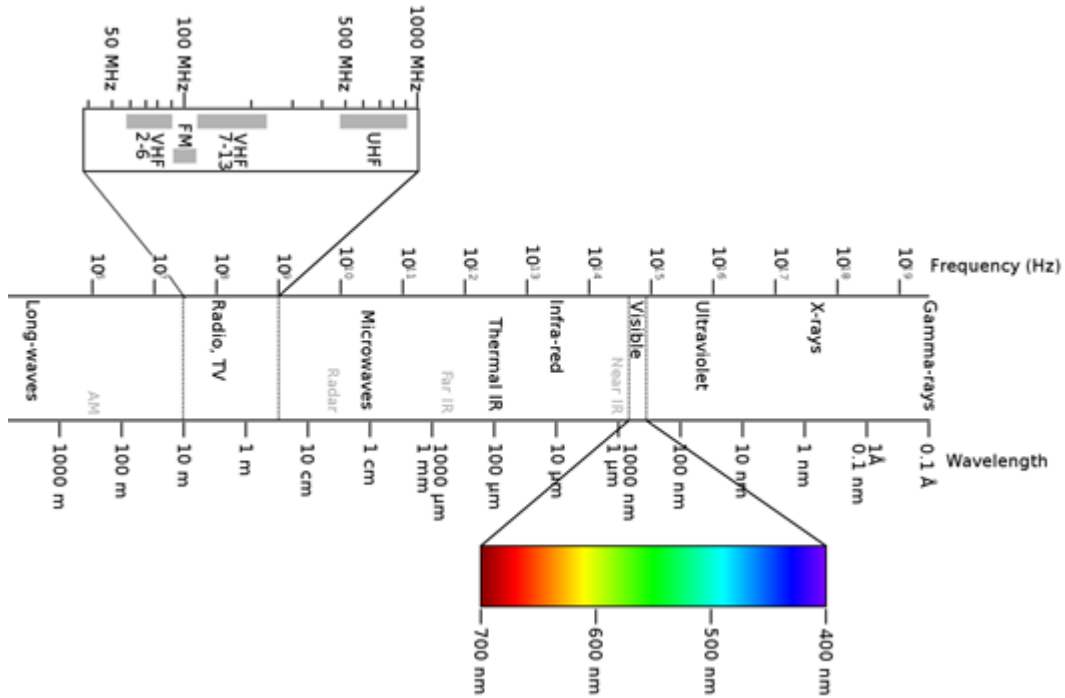
Figure 3.3: Electromagnetic Spectrum division (taken from Wikimedia Commons under CC BY-SA 2.5 license).

[μm] or [nm], while for the wavenumber [$1/m$].

Monochromatic intensity (spectral intensity or monochromatic radiance) and Intensity (or radiance).

The monochromatic intensity I_λ (I_ν) is defined as the amount of radiation by solid angle unit for each wavelength in the spectrum. Its unit is [$\frac{W}{m^2 sr}$]. The integral of the monochromatic intensity over a range of wavelength, frequency, or wavenumber is called intensity I, and its unit is also [$\frac{W}{m^2 sr}$].

Definition 3.1 *Monochromatic intensity*

$$I = \int_{\lambda_1}^{\lambda_2} I_\lambda \mathrm{d}\lambda = \int_{\nu_1}^{\nu_2} I_\nu \mathrm{d}\nu$$

From the definition in Definition 3.1 is possible to demonstrate that

$$I_\nu = \lambda^2 I_\lambda \tag{3.2}$$

Which is the relation between the monochromatic intensity defined from the wavelength and the wavenumber.

11

Incident Monochromatic flux density (monochromatic flux radiance) and incident Flux density (or irradiance).

The incident monochromatic flux density F_λ is defined as the amount of monochromatic intensity incident over a surface from all directions in units of $[\frac{W}{m^2 \mu m}]$. Thus:

Definition 3.2 *Incident Monochromatic flux density*

$$F_\lambda = \int_{2\pi} I_\lambda cos\theta \mathrm{d}\omega$$

$\mathrm{d}\omega$ is the element of solid angle, and $cos\omega$ is the normal angle to the surface. Similar to the monochromatic intensity, the incident flux density is defined as:

$$F = \int_{2\pi} I cos\theta \mathrm{d}\omega = \int_{\lambda_1}^{\lambda_2} \int_{2\pi} I_\lambda cos\theta \mathrm{d}\omega \mathrm{d}\lambda \tag{3.3}$$

For the sun photometer developed in this work, the Sun will be used as the primary radiation source. Under this case, the flux of solar radiation E_s is constant for each sphere centered in the Sun. Then:

$$E_s = F_s \times 4\pi \mathrm{d}^2 = constant \tag{3.4}$$

Thus, the incident flux intensity from the Sun decreases with the square of the distance. Finally, E_s can also be obtained from monochromatic intensity by the following procedure:

$$E_s = \int_{\delta A} \int_{2\pi} \int_{\lambda_1}^{\lambda_2} I_\lambda(\phi, \theta) \mathrm{d}\lambda cos\theta \mathrm{d}\omega \mathrm{d}A \quad [W] \tag{3.5}$$

In this equation, ϕ and θ are angles in spherical coordinates.

3.2.2. Radiation physics

This section presents the effect that the atmosphere has over the solar radiation, which defines the Aerosol Optical Depth (AOD). First, the definitions exhibited in the previous section are used to enunciate some physical proprieties of the radiation. Then, how the radiation interacts with the atmosphere is explained. Finally, the AOD is defined.

The black-body radiation

A black-body is a theoretical body with specific radiation properties. It is defined as a perfect emitter and absorber of radiation, i.e., neither other surface nor body can emit as much energy as a black-body given any temperature and wavelength. Another property of a black-body is that it emits uniformly in all directions. That means a black-body is fuzzy [24]. In the following, all radiative properties will be defined considering a black-body.

The Planck's function or Planck's Law.

This law defines the spectral emission power of a black-body. It was found experimentally by Max Planck, and it refers to the quantity of radiation energy emitted by a black-body given an absolute temperature T per time unit, surface area, and wavelength. Moreover, because a black-body is defined as fuzzy, it is possible to calculate the intensity of radiation of a black-body. The definition in Eq. 3.3 is the Planck's Law, while the definition in Eq. 3.4 is the intensity of radiation,also called the Planck's function[22].

Definition 3.3 *Planck's Law*

$$F_{b\lambda}(\lambda, T) = \frac{C_1}{\lambda^5 [exp(\frac{C_2}{\lambda T}) - 1]} \quad [\frac{W}{m^2 \mu m}]$$

Where:

$$C_1 = 2\pi h c_0 = 3.74177 \times 10^8 \quad \frac{W \cdot \mu m^4}{m^2}$$

$$C_2 = \frac{h c_0}{k} = 1.43878 \times 10^4 \quad \mu m \cdot K$$

Definition 3.4 *Planck's function*

$$B_\lambda(\lambda, T) = \frac{c_1 \lambda^{-5}}{\pi [exp(\frac{c_2}{\lambda T}) - 1]} \quad (\frac{W}{m^2 \cdot \mu m \cdot sr})$$

Where:

$$c_1 = 3.74 \times 10^{-16} \quad W \cdot m^2$$

$$c_2 = 1.45 \times 10^{-2} \quad m \cdot K$$

In all the equation above T is the temperature in $[K]$, λ is the wavelength in $[\mu m]$, $h = 6.621 \times 10^{-34}$ $[J \cdot s]$ is the Planck's constant, $c_0 = 299792458[\frac{m}{s}]$ is the speed of the light and $k = 1.38065 \times 10^{-23}$ $[\frac{J}{K}]$ is the Boltzmann's constant.

The Wien's displacement law

The wavelength where the emission is maximal is found, deriving the Planck's law and making the result equal to zero. This result is known as the Wien's displacement law and is shown in the Eq. 3.6. It is possible to notice that the maximal emission wavelength is inversely proportional to the temperature T.

$$(\lambda T)_{maxpower} = 2897.8 \quad [\mu m \cdot K] \tag{3.6}$$

The Stefan-Boltzmann Law

Integrating Planck's law is possible to obtain a black body's emission power (or flux density). This result is known as the Stefan-Boltzmann law. Finally, $\sigma = 5.670 \times 10^{-8}$ $[\frac{W}{m^2 \cdot K^4}]$ is the Stefan-Boltzmann constant and T is the temperature of the surface in $[K]$. The Eq. 3.7 shows the Stefan-Boltzmann Law.

$$F = \sigma T^4 \quad [\frac{W}{m^2}] \tag{3.7}$$

The Sun can be modeled as a black-body with a surface temperature of 5780 K. This assumption is accurate considering visible, and near-visible spectral bands [25]. To complete this section, it will define the radiative proprieties of a non-black material and the Kirchhoff's Law.

Radiative properties of non-black materials.

The properties of non-black materials are defined using the black-body definition. Instead of absorbing and emitting all the radiation, the non-black material not only absorbs radiation but also can transmit and reflect energy. For that reason, it is necessary to define the monochromatic emissivity ε_λ as the rate of monochromatic intensity emitted with respect to the black-body (the theoretical maximal monochromatic intensity for a given temperature and a wavelength). From the above, it follows that $\varepsilon_\lambda \in [0;1]$. The definition is shown formally in the Eq. 3.8.

$$\varepsilon_\lambda = \frac{I_\lambda(emitted)}{B_\lambda(\lambda, T)} \tag{3.8}$$

Therefore, a nonblack material can absorb, reflect, and transmit radiation. For this reason, it is convenient to define the monochromatic absorptivity α_λ, reflectivity R_λ, and transitivity T_λ as the rate of energy of absorbing, reflecting, and transmitting with the incident monochromatic intensity. Similar to ε_λ; α_λ, R_λ and $T_\lambda \in [0;1]$.

$$\alpha_\lambda = \frac{I_\lambda(absorbed)}{I_\lambda(emitted)} \tag{3.9}$$

$$R_\lambda = \frac{I_\lambda(reflected)}{I_\lambda(emitted)} \tag{3.10}$$

$$T_\lambda = \frac{I_\lambda(Transmitted)}{I_\lambda(emitted)} \tag{3.11}$$

The Kirchhoff's Law.

This law establishes that under thermal equilibrium, the emissivity and the absorptivity have the same value. At this point, the radiator is assumed as a small body in order to

neglect other heat transfer processes. Therefore, the incident intensity will be the same as a black-body with temperature T following Stefan-Boltzmann's Law. Thus, the absorbed radiation and the emissivity are defined by the Eq. 3.12.

$$A_s \varepsilon \sigma T^4 = A_s \alpha \sigma T^4 \tag{3.12}$$

Where A_s is the surface of the small body, σ and α are the emissivity and the absorptivity, respectively. Simplifying The Formula 3.12, it is concluded that under thermal equilibrium, $\varepsilon = \alpha$.

Kirchhoff's Law is used in a simple model of the radiation balance of the atmosphere. It is used in models like the multi-layer thermal equilibrium atmosphere model to describe the first-order balance of radiation. As mentioned before, solar radiation can be modeled as a black-body. In contrast, atmosphere interaction with radiation can widely be modeled as a black body given that particles and gases are able to absorb and scatter radiation, as we will see in the next section.

3.2.3. Scattering and absorption physics in atmosphere.

The Sun can be considered as a black body. However, the radiation spectrum in the Earth's surface has some differences from a black-body spectrum, as shown in Figure 3.4. The atmosphere cannot be modeled as a black-body, i.e., the air can absorb, reflect, and transmit radiation as the air is a mixture of components, such as oxygen, nitrogen, and other gas molecules (CO_2, Ar, Water vapor, and other), and aerosols. The amount and composition of the atmosphere affect the radiation detected on the ground.
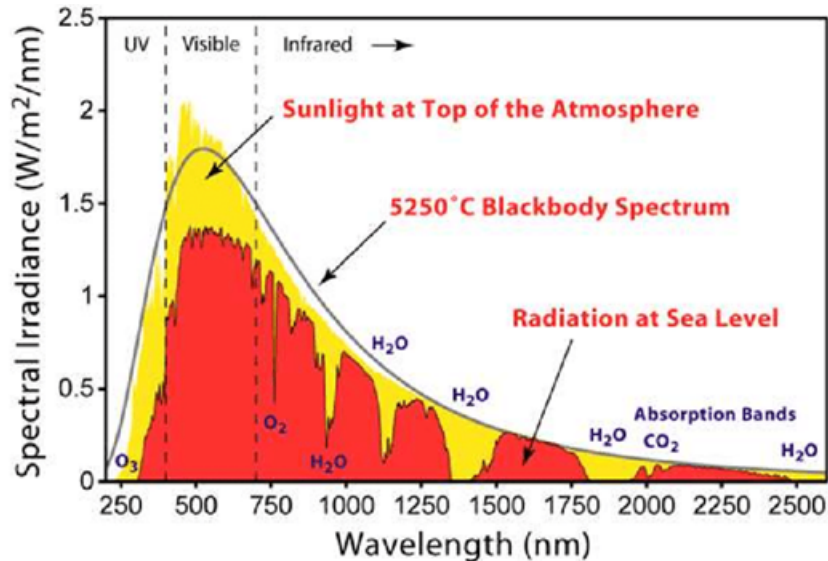
Figure 3.4: Solar spectrum and Atmospheric radiation spectrum in the surface of the Earth (taken from Wikimedia Commons under CC BY-SA 3.0 license).

Figure 3.4 also exhibits that individual constituents can absorb radiation at a specific wavelength. One example of that is the ozone properties to absorb UV radiation. Another

example is the capacity of CO_2 to absorb and reflect infra-red radiation. In the visible spectrum, the main absorbers of light in the atmosphere are water vapor with 27 reported narrow absorption bands in the visible spectrum, and the ozone with the Chappuis, which covers the electromagnetic spectrum between 450 and 750 nm [25].

In this section, an overview of the radiation properties in the atmosphere is presented. Focusing on the scattering into the atmosphere and finally defining the Aerosol Optical Depth (AOD).

Scattering in the atmosphere

Scattering refers to the re-emission of light in different directions and intensity of incident light. Both abortion and scattering contribute to the extinction of solar light. The extinction has three proportional dependencies:

1. The intensity of radiation at that point along to the ray path.
2. The local concentration of gases and particles responsible for the absorption or scattering.
3. The effectiveness of the absorbers or scatters

The relations presented before can be summarized in the differential monochromatic intensity showed in the following Formula [22]:

$$dI_\lambda = -I_\lambda K_\lambda N \sigma ds \tag{3.13}$$

Where I_λ is the monochromatic intensity, K_λ is the scattering or absorption efficiency (dimensionless), N is the number of particles per unit of volume, σ is the areal cross-section of the particles, and ds is the differential path length along the ray path of incident radiation. The contributions from different kinds of gases or particles are additive. Finally, the total efficiency can be decomposed as adding scattering and absorption efficiency.

The air molecules' scattering regime or particles in the atmosphere depend mainly on the particle size regarding to the wavelength. Thus, three kinds of radiation modes are recognized:

- Rayleigh mode if the particle size is much smaller than the incident wavelength.
- Mie mode if the particle size is similar to the incident wavelength.
- Optical mode if the particle size is larger than the incident wavelength.

The size parameter is defined as the rate between the equivalent circular perimeter of the particle and the wavelength to compare the particle size and the incident wavelength. How both parts have length units, the size parameter is dimensionless. Thus:

$$x = \frac{2\pi r}{\lambda} \tag{3.14}$$

Where r is the equivalent radius of the particle.

Another variable in consideration is called the complex index of refraction $m = m_r + im_i$, where the real part is the rate between the light's speed inside the particle and the light's speed in the vacuum. While m_i is related to the attenuation coefficient. When $m_i = 0$ means there is not absorption.

In the following, Rayleigh, Mie, and optical scattering modes are described. The first is related to the air molecules' optical depth contribution, which is an important parameter to determine AOD. Simultaneously, Mie and optical modes are related to aerosols' contributions, as larger particles in the atmosphere, to the optical depth.

Rayleigh mode or scattering.

The Rayleigh scattering occurs when an electromagnetic wave passes through a particle, and the particle size is much smaller than the incident wavelength, which is $x << 1$. That is the case of the air molecules with the visible (or near-visible) wavelength. The Rayleigh mode is characterized by a scattering efficiency inversely proportional to the fourth power of the wavelength, as follows in the Formula 3.15

$$K_\lambda \quad \alpha \quad \lambda^{-4} \tag{3.15}$$

Mie mode or Mie scattering

The Mie scattering is considered when $0.1 \leq x \leq 50$ and is characterized by a damped oscillatory behavior of the scattering efficiency K_λ. The mean value of the efficiency is 2, as it is shown in Figure 3.5. For $x > 50$ the oscillatory behavior can be neglected and consider the geometric optics regime with $K_\lambda \approx 2$.
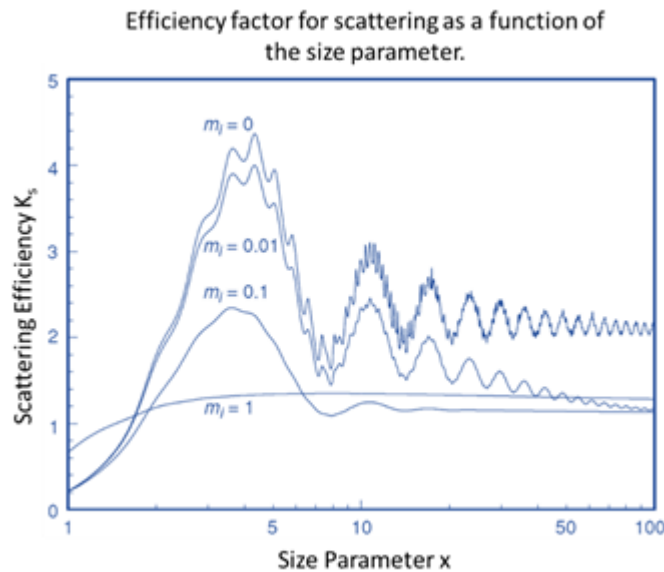
Figure 3.5: Efficiency factor for scattering as a function of the size parameter. Notice the dumped behavior of the scattering efficiency to parameter size under 50 (Adapted from Liou, (2002)).

Optical mode or Optics

When the particle size is larger than the wavelength, the scattering behavior can be modeled using the classical optics theory. It is possible to distinguish between different ray paths in different parts of the surface of the particle. Figure 3.6 [26] shows an example of that.
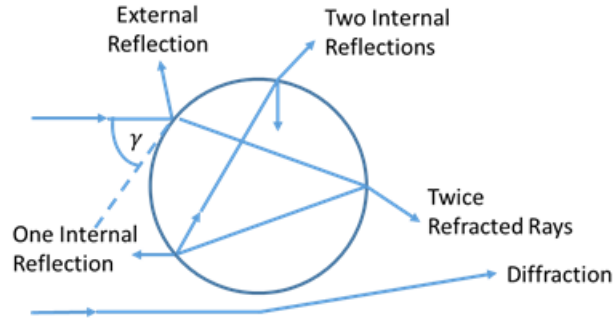
Figure 3.6: Paths of light rays scattered by a sphere according to geometrical optics (Adapted from Hansen et al. (1974))

Another important aspect to consider in the particles' scattering is the angular distribution of the incident radiation. This distribution can be divided into the forward and backward hemisphere. Figure 3.7 shows the angular distribution for a visible wavelength and different particle sizes.
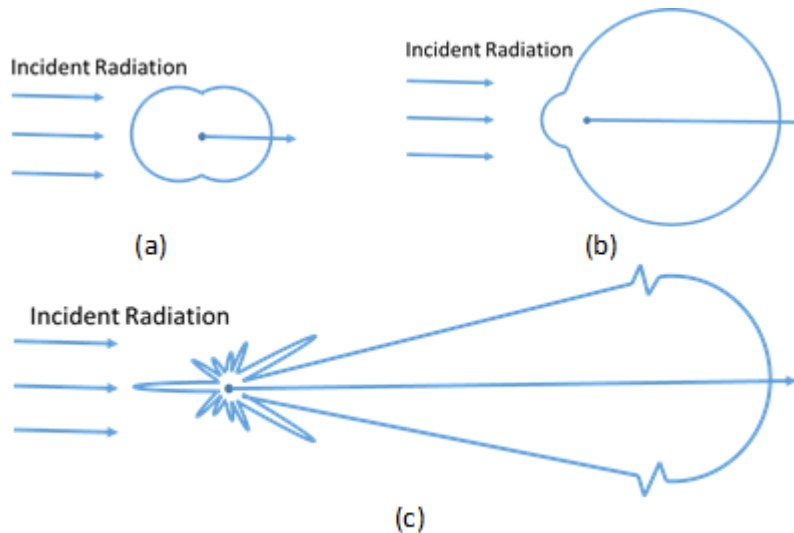
Figure 3.7: Angular patterns of the scattered intensity from spherical aerosols of three sizes illuminated by the visible light of 0.5 μm: (a) $10^{-4}\mu m$ (Rayleigh mode) (b) 0.1 μm, and (c) 1 μm (Mie mode). The forward scattering pattern for the 1 μm aerosol is extremely large and is scaled for presentation purposes (Adapted from Liou, (2002)).

Figure 3.7, Small particles (Rayleigh scattering) are relatively ineffective at scattering radiation and have a homogeneous angular distribution in both hemispheres. However, large

particles (Mie Scattering) are more efficient at scattering, and the angular distribution prefers the forward hemisphere. In the next section, we present the Beer-Lambert-Bouguer's Law. It describes how the monochromatic Intensity decreased through the atmosphere, and finally, the Optical Depth is defined.

Beer-Lambert-Bouguer's (BLB) Law and Aerosol Optical Depth.

This Law was found independently by Pierre Bouguer (1729), Johann Heinrich Lambert (1760), and August Beer (1852), and it exhibits how the monochromatic intensity is extinguished by the atmosphere (air molecules, aerosols, and other gases). In this section, It is defined the BLB's Law from the definitions presented in previous sections. After that, we describe the optical depth and explore its different constituents.

In the previous section, the differential monochromatic intensity was presented in the Eq. 3.13. Integrating from the top of the atmosphere to measurement place on the ground, following the ray path. It is possible to define the monochromatic intensity received on that point, as shown in the next equation:

$$ln(I_{\lambda\infty}) - ln(I_\lambda) = \int_s^\infty K_\lambda N\sigma \mathrm{d}s) \tag{3.16}$$

Where $I_{\lambda\infty}$ is the monochromatic intensity at the top of the atmosphere, we use $\mathrm{d}s = m\mathrm{d}z$, where m is the air mass, and $\mathrm{d}z$ is the differential altitude from the measurement's position to the top of the atmosphere. The Eq. 3.16 can be rewritten as Eq. 3.17.

$$ln(I_{\lambda\infty}) - ln(I_\lambda) = m \int_s^\infty K_\lambda N \mathrm{d}z \tag{3.17}$$

Applying the antilog and reorganizing Eq. 3.17 is possible to obtain the monochromatic intensity at the point of measurement.

$$I_\lambda = I_{\lambda\infty}exp(-m \int_s^\infty K_\lambda N \mathrm{d}z = I_{\lambda\infty}exp(-m\tau_\lambda) \tag{3.18}$$

Eq. 3.16 is a strength definition of BLB's Law, which does not consider the variation of the distance between the sun and the Earth. The monochromatic intensity at the top of the atmosphere depends on this distance. Therefore, the equation can be corrected as follows:

$$I_\lambda = \frac{I_{\lambda_0\infty}}{r^2}exp(-m \int_s^\infty K_\lambda N \mathrm{d}z = \frac{I_{\lambda_0\infty}}{r^2}exp(-m\tau_\lambda) \tag{3.19}$$

In this equation, $I_{\lambda_0\infty}$ is the monochromatic intensity at a distance between the Earth and The Sun of $1AU$ [9]. r is the distance Earth-Sun in AU at the moment of the measurement. From Eq. 3.19 is possible to define the Optical Depth (OD) as follows:

$$\tau_\lambda = \int_s^\infty K_\lambda N \mathrm{d}z \tag{3.20}$$

The Optical Depth is the rate of depletion (in logarithmic scale) of monochromatic radiance caused in an airmass column. The extinction has mainly three contributors: air molecules (Rayleigh scattering), absorption of certain gases, and absorption and scattering by aerosols. Therefore, the OD can be separated as:

$$\tau_\lambda = \tau_{\lambda r} + \tau_{\lambda g} + \tau_{\lambda a} \tag{3.21}$$

$\tau_{\lambda r}$ is the Rayleigh Scattering (RS), which depends on the wavelength and the height of the place of the measurement, represented as a ratio of atmospheric pressure between the local measurement place and the sea level. It could be estimated using the procedure presented by [27].

$\tau_\lambda g$ is the Gas Absorption Optical Depth (GAOD), and it corresponds to the absorption of radiation of certain gases at some wavelengths. It is assumed that the gases' effect is negligible at the wavelength used in this work because the used sensor has a spectral approximately response between 350 nm and 450 nm, not covering the Chappuis absorption band and water band are too narrow to be considered in the measurement [25].

$\tau_{\lambda a}$ is the Aerosol Optical Depth (AOD). It corresponds to the depletion radiation rate caused by aerosols in the atmosphere.

In this work, the main goal is the measurement of the AOD. To do so, if the measurement is performed over a wavelength band, it will be necessary to discount the measure of the contribution from the RS and GAOD. In the methodology section is described the procedure used to estimate and neglect these sources of depletion. In the next section are presented some instruments used to estimate the AOD.

3.3.   AOD measurement instruments.

In this section, the main instruments used for AOD measurement are described. It is briefly described the LIDAR and satellite radiometers. Later, the Sun Photometer is explained, focusing on the necessary elements to define the instrument's measurement procedure developed in this work.

3.3.1.   LIDAR

The *Light Detection And Ranging* (LIDAR) is an active instrument that emits a narrow wavelength band (near to monochromatic) light using a laser, measuring the returned light from the atmosphere using a photo-diode. It is possible to estimate the AOD at that wavelength band using certain corrections. Figure 3.8 shows a simple configuration of a LIDAR.

The LIDARs' main advantages are: (1) it can be exact and (2) it can be used at night.
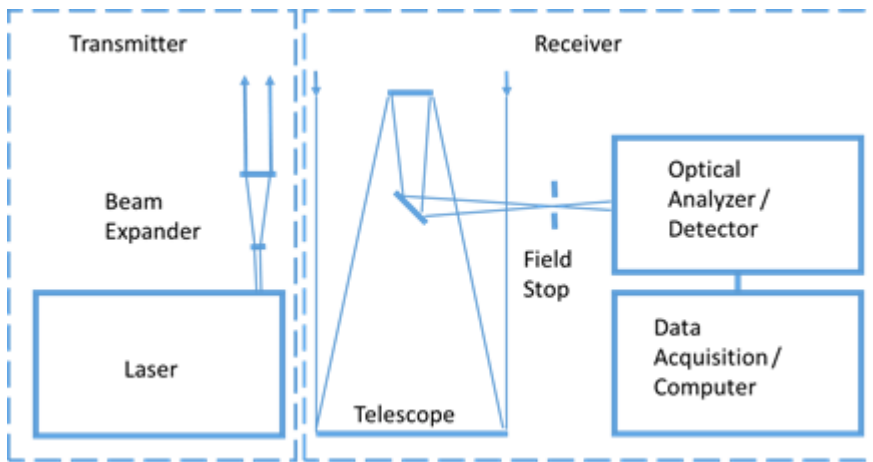
Figure 3.8: Principle setup of a LIDAR system (Adapted from Weitkamp, (2006)).

However, the main disadvantage is its cost compared to other alternatives, in particular the Sun Photometers.

3.3.2.   Satellite Radiometer

Although some LIDARs are mounted in satellites (for example, CALIOP in CALIPSO satellite), there is a passive instrument called radiometers, more commonly used as the payload in satellites. This instrument also uses a narrow light band (near monochromatic) to estimate the AOD. This method's main difficulty is that the radiometer detected signal is the Sun's light reflected from the Earth's surface. It is then necessary to perform procedures, usually involving calibrations, to estimate the AOD since it requires estimating the Earth's surface's reflection to retrieve the AOD. Figure 3.9 shows an example of a Satellite instrument.

Figure 3.9: Example of Satellite taking measurements from the Earth. In this case is the Sentinel-5 Precursor satellite, which has the TROPOMI radiometer. AOD products are developed from the data obtained by this satellite (taken from Wikimedia Commons under CC BY 3.0 license).

The main advantage of this kind of instrument is the spatial resolution since it is possible to take measurements from the whole Earth (in a Low Elliptic Orbit (LEO)) or a large

portion of the Earth part (in the case of the geostationary orbit (GEO) satellites). The main disadvantages of the instrument are: (1) the lower precision of the measurement compared to those taken by ground instruments and (2) that the area covered by a pixel of the radiometer can include several square kilometers [5]. Another problem in an LEO satellite radiometer is the sampling since the satellite revisits the same place only a few times per day. MODIS are radiometers used in two satellite missions (Terra and Aqua).

3.3.3.   Sun Photometers.

A Sun Photometer consists of a passive instrument with a photo-diode in a narrow wavelength band aligned with the Sun to take AOD measures. The measure is corrected by subtracting the RS and GAOD. This instrument's main advantages are: (1) the precision of the measurement and (2) the temporal resolution compared with satellites. This instrument's challenges are: (1) the need to point and track the Sun for each measurement and (2) that the price of automated systems makes it challenging to increase the spatial resolution with this kind of instrument.

Examples of commercial Sun Photometers are Cimel, Microtops, Calitoo, and the GLOBE program's Sun Photometer. Other examples of Sun Photometers are the Toledo et al. (2018) Sun Photometer, and the miniASP [15]. Figure 3.10 Shows a Cimel Sun Photometer during operations, and Table 3.1 summarizes the main features of the Cimel instrument. This instrument is an automatic Sun Photometer and is considered as the ground truth device to measure AOD.

Figure 3.10: Cimel Sun Photometer (Santiago Beauchef station) taking measurements.

Number of channels	8
Wavelengths λ [4]	340 nm / 440 nm / 670 nm / 870 nm / 940 nm / 1020 nm
Measurement type [4]	1 measurement (triplet) each 5 or 10 minutes depending of the model
Measurement process [4]	3 measurement per channel each 30 seconds ($\sim$1 second per individual measurement)
Average variability of a triplet [4]	Less than 1% (typically 0.3%)
Servo motor precision to automatic tracking [4]	0.05º
Sun Position Algorithm precision [4]	1º
Calibration coefficient variation (CV) (standard deviation/mean) [4]	visible and near-IR: $\sim$ 0.25%-0.50% / UV: $\sim$ 0.5%-2% water vapor channel $\sim$ 1%-3% water vapor channel
Accuracy (after calibration)	$\pm$0.1 for $\lambda > 440nm$ and $\pm$0.02 for $\lambda \leq 440nm$ [4] $\pm$0.01 for all wavelengths [6]

Table 3.1: AERONET Cimel Sun Photometer main features

Chapter 4

Methodology

An automatic Sun Photometer was developed to take AOD city-scale measurements. The main objectives of the instruments are: (1) to explore the feasibility of implementing an automatic city-scale network to measure AOD, (2) to use the variation of the AOD at this scale to understand better the behavior and dynamics of the aerosols in an urban area such as Santiago de Chile.

Agile manufacturing was considered for the development of the instrument. The approach followed by this project was inspired by other agile designs and manufacturing programs, such as The Gossamer Condor aircraft [28]. The philosophy of the project followed these main drivers:

- The hardware must permit quick repairs and modifications.

- To focus on the automatic Sun tracking system, assuming that the AOD sensors work correctly and operational issues would be solved in future iterations.

- Informal project management and System engineering, focusing on field tests to validate the instrument and only documenting the validated requirements of the project

Figure 4.1 shows an overview of the instrument development process. First, the requirements of the instrument were defined. With them, the requirements of each subsystem and the testing criteria to reach the requirements were established. Thus, simple prototypes of each subsystem were designed (schematized) and developed. Then, each subsystem prototype was tested. Based on the test performance of each subsystem, changes and improvements were proposed to the previous designs. Through this iterative process, a final prototype was reached along with this work.

This process has three main advantages: (1) To achieve the instrument low-cost constraint in the design because the capabilities are increased only when a component fails, not overestimating the capabilities of the instrument. (2) To validate the components of the device under real operation conditions. (3) Save time, not documenting changes that were not present in the final design.

The design of an instrument requires overcoming several challenges. For example, define
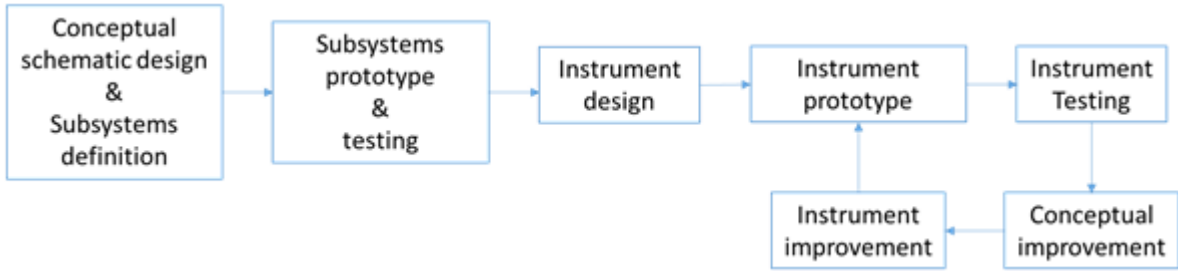
Figure 4.1: Instrument design and construction methodology.

the subsystems, building, testing, and integrate them to form the instrument, among many and others. Moreover, the automatic operation of a city-scale Sun Photometer network imposes specific requirements to facilitate operations. In the first part, the instrument is described, highlighting the requirements that define the design decisions. The second part exhibits the AOD estimation processes in detail, including the calibration procedure and campaigns, and a city-scale campaign to exemplify the measurement concept.

4.1.   Instrument development.

The goal is to design a low cost and automated prototype. It must take measurements without human intervention. That means the instrument has to detect the Sun and follow it to measure. Furthermore, each instrument must overlap measurements with others over a long time and save the measurement information. 4.1 summarizes the desired requirements for the Sun Photometer prototype.

1. Technical Requirements	
1.1.	Use of commercial components (Commercial off-the-shelf (COTS))
1.2.	Low cost of the instrument (Under 300 USD in components)
1.3.	Easy replacements and testing of components (Agile manufacturing)
1.4.	Consistent manufacturing
2. Operational Requirements	
2.1.	Autonomous tracking of the Sun
2.2.	Low power consumption
2.3.	Only operates during the day
2.4.	Resistant to heat and water proof (Final version)

Table 4.1: Initial Requirements for the prototypes

The technical requirements include the use of low-cost commercial components and easy to replace and test. These requirements are necessary with two goals: (1) to develop the instrument using agile manufacturing and continuous improvements of the instrument, incorporating capabilities and progress over time. (2) Keep the instrument's cost low, using only the necessary qualifications of components to the instrument (not overestimate the instrument requirements). Finally, a consistent manufacturing requirement is required to produce several units with identical capabilities.

The operational requirements are related to the network operation. The autonomous Sun

tracking, low power consumption, and daily operation are needed because the instrument must measure alone without intense human supervision. The last desired requirement (2.4 in 4.1) will be considered after evaluating the instrument's measurement performance.

Previous experience with this instrument was the Sun Photometer developed by Toledo et al. (2018). This instrument is based on the Brooks et al. (2001) handheld Sun Photometer and uses Light Emitting Diodes (LEDs) working as low-cost light detectors. However, this instrument is human-operated, can take measures and save it. Figure 4.2 shows a schematic design and a picture from the Toledo et al. (2018) Sun Photometer.
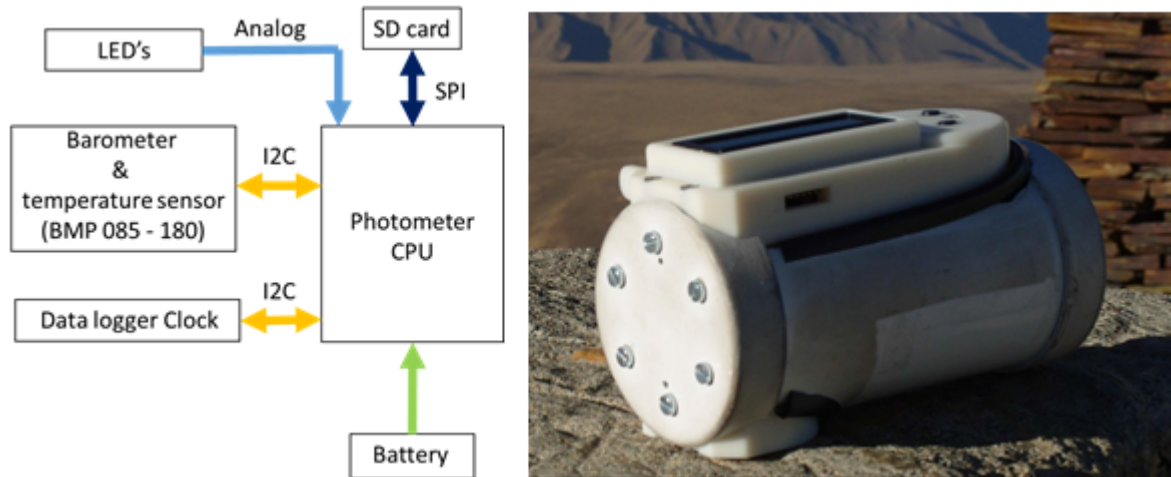
Figure 4.2: Instrument design and construction methodology.

4.1.1. Conceptual schematic design and subsystem definition.

The first stage is the conceptual schematic design and the definition of all the subsystems: From the Toledo et al. (2018) Sun Photometer and adding the new requirements. Our prototype tried to keep the Toledo et al. (2018) Sun Photometer conceptual design core inside our new conceptual design, only applying some hardware improvements to it. Furthermore, the conceptual design considered some possible future improvements over the prototype.

The result of this approach, the automated control of the instrument was considered a separate system. That system must turn on/off the Sun Photometer, align it with the Sun, and inform the instrument when to start to measure. Figure 4.3 shows the conceptual design of this new instrument.

Comparing this design with Toledo et al. (2018) Sun Photometers, some subsystems have several differences. The main improvement was replacing the sensor acquisition from an analog interface to a Serial Peripheral Interface (SPI). With that change, the sensor resolution is increased.

Another change is the clock's replacement from an RTC (Real Time Clock) to a GPS. That means all the Sun Photometers in the network have the same time everywhere, instead of Toledo et al. (2018) Sun Photometer, where the time was synchronized manually by the users. Finally, the last change is the possibility of add a GSM transceiver. With this,

the instrument could send housekeeping and measurement data over the cellphone network. Table 4.2 compares in detail all the improvements of the instrument.

The Sun tracker system includes an alarm clock to indicate when the instrument must measure and an energy controller to switch on/off the instrument and the motors when they are unused. The solar sensor is used by the Sun tracker to find the Sun and align the AOD sensor with the Sun using the servo motors.
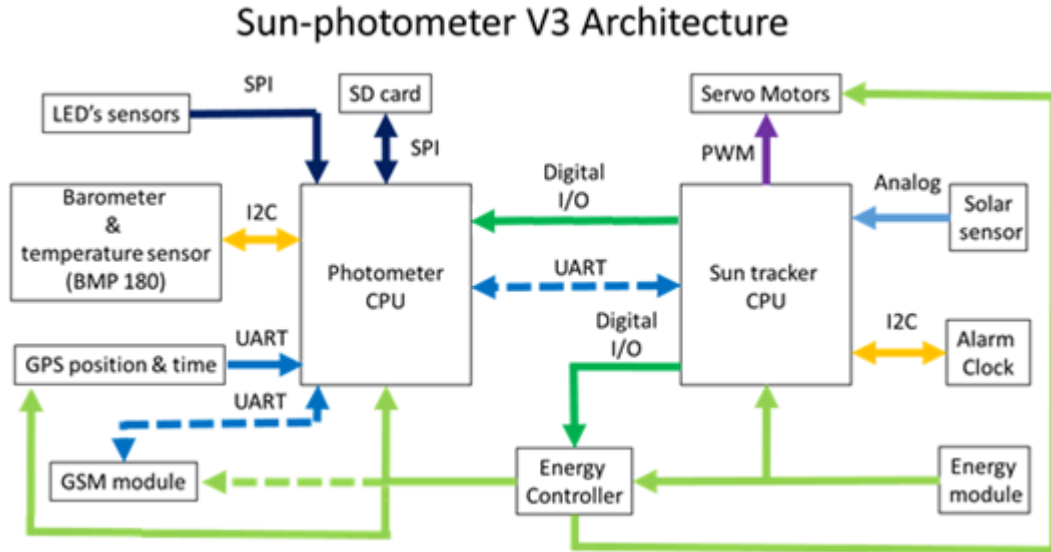
Figure 4.3: Schematic design for our Sun Photometer.

From 4.3, each component must be designed, build, and tested. Once each part is consolidated, all of the pieces must be integrated into the instrument. Finally, the instrument must be tested and improved using the results of the tests.

4.1.2. Subsystems prototyping and operational verification of them.

At an early stage, potential components were selected and individually tested. With this information, the subsystem models were made and evaluated. Most of these subsystem prototypes used proto-boards and basic connections such as cables to test the subsystems and components' operation performance. Like the GPS-GSM module, other elements are bought and tested to know how it works and if it can be integrated into the instrument.

Even though the subsystems are tested individually, the inter-subsystem connectivity must be considered at this stage to avoid possible compatibility issues among subsystems. Figure 4.4 shows a typical set of some subsystems connected.

4.1.3. Instrument Design

This stage consisted of designing the first integration of subsystems in an instrument prototype, considering all the electronic and mechanical parts. Figure 4.5 shows some components and subsystems at this stage. The mechanical parts were designed using SOLIDWORKS 2017 [29], while all the PCBs were designed using KiCAD 4 [30].
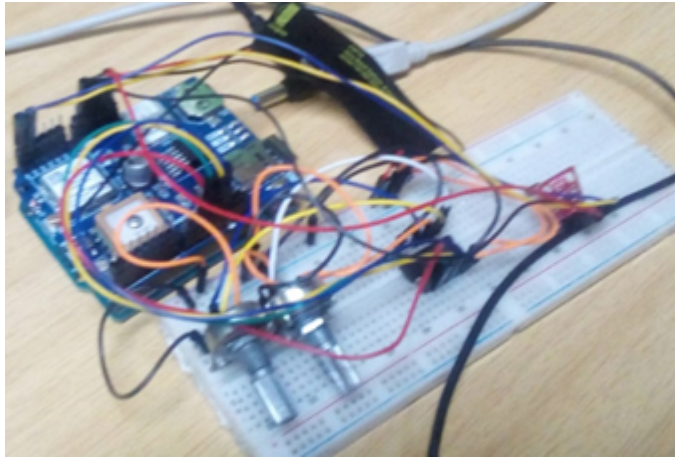
Figure 4.4: Different subsystems prototype connected under testing.
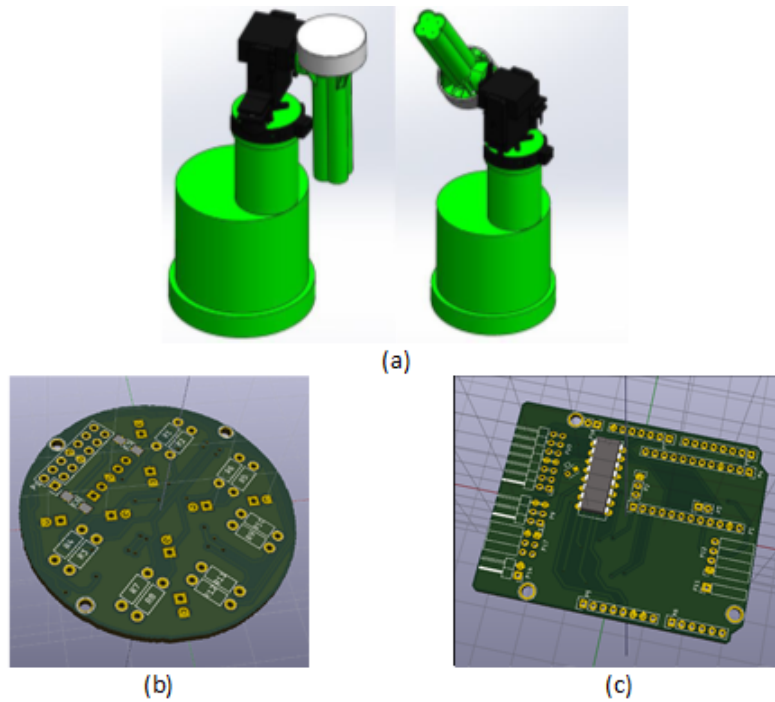
Figure 4.5: Design of different components of the instrument. (a) CAD view of the instrument. (b) Sensor PCB design and (c) Energy and robotic arm PCB.

4.1.4. Instrument prototype

After the design stage, the first prototype unit of the instrument was built. Figure 4.6 displays the same designed parts showed in Figure 4.5, after the construction. The details of the prototype will be presented only for the last version of it.

The first version of the instrument only considered the working of each component individually. For that reason, an integration of all the parts through the software was needed to achieve the device's requirements and obtain AOD measurements. Furthermore, software development and improvement could improve and add new capabilities to the instrument
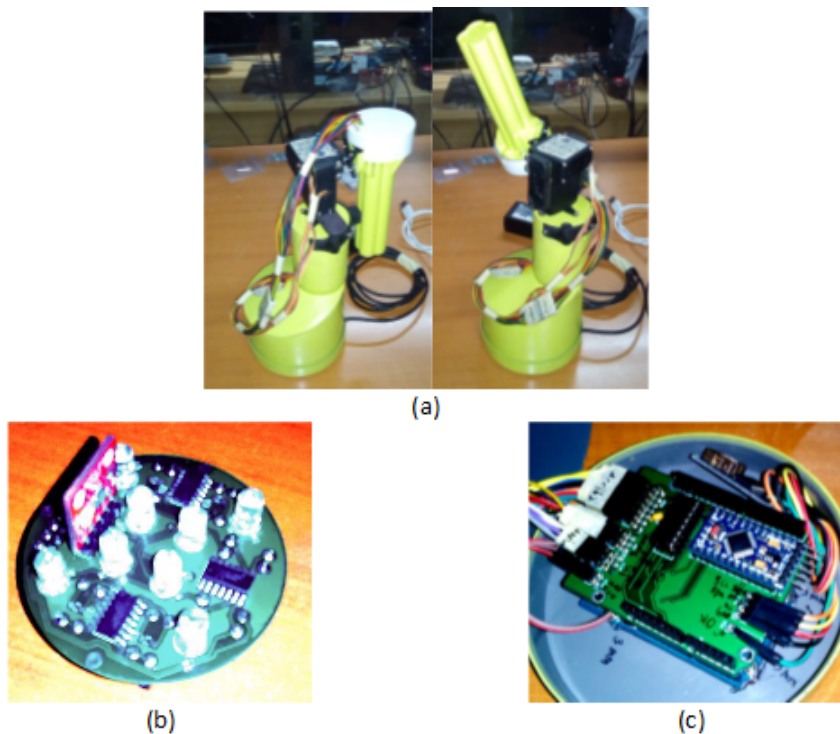
Figure 4.6: Different components of the first version of the prototype. (a) Main view of the instrument. (b) Sensor PCB and (c) Energy and robotic arm PCB.

through iterations.

The instrument testing consisted of taking measurements under real environmental conditions. That means, first try to find the Sun, then capture the AOD sensor response and save all the data into the μSD card. From this process, the software was improved from the observation of the behavior of the instrument. In addition, some of the weaknesses of components were noticed. Based on the test results, changes to the design were proposed. Figure 4.7 shows the first instrument under testing. The Sun-tracking capability of the instrument proved to be operational at this stage, but with some issues.

The number of iterations cycles is undetermined because the modifications were decreasing during the process. In the first cycle, all the Sun tracking system hardware must be redesigned. In the following cycles, only small modifications were introduced, such as the replacement of a wire. Once the instrument hardware was consolidated, only the software continues under the cycle. The frequency of the modification also decreased over time. In the beginning, almost every weakness of the instrument was modified. In the last part, the software was modified once a year.

The major obstacles of the prototyping process were the new capabilities of the instrument. While the improved capabilities inherited by Toledo et al. (2018) [10] Sun Photometer just required one cycle to be functional, the components with less knowledge required significant efforts. Another important challenge was the integration process of all the components of the instrument and the software. Before the integration, each component could work individually, but some components' functions stopped working after integration. Several modifications

were required in the software to make all the components work together.

Figure 4.7: First version of the prototype tracking the Sun.

4.1.5. Instrument improvement

These last two stages consist of proposing the changes to the prototype and execute them. For example, after the prototype testing, the servo motors were not reliable enough to track the Sun because they tried to use 360° velocity control servo motors without position control. Therefore, the mechanical part of the Sun tracker should be improved. The result was that the servo motors were replaced from velocity control servos to position control servos, and the design of the Sun tracker mechanical part was improved, changing the form of the obstacles that cover the light sensors when the instrument is not aligned with the Sun.

After applying the changes, the test and verification stage was performed again to verify the operation. Finally, when a stable version of the instrument was consolidated, the other prototypes' production started.

Figure 4.8 shows the stable developed Sun Photometer prototype and its components. It is essential to highlight that the instrument looks very similar to the version of the instrument presented in Figure 4.7. The reason for that is because most changes after site tests were performed in software, while the hardware only had incremental improvements.

4.2. Components of the Sun Photometer.

The instrument could be decomposed into two main subsystems: the Sun Photometer and the Sun tracker. Each subsystem is controlled by an ATmega 328p CPU (Arduino). Although the conceptual schematic presented in Figure 4.3 considers independent subsystems in the instrument, some designed parts share the capabilities of both. For example, the Sun Photometer sensor PCB in Figure 4.8 have the AOD sensors from the Sun Photometer and the Sun position sensors from the Sun Tracker system to assure a proper alignment of the sensors whit the Sun. Figure 4.9 shows how the components are distributed into the two central systems and also the parts where they belong in the instrument showed in Figure 4.8. In this section, the detail of each part of the instrument is explained.
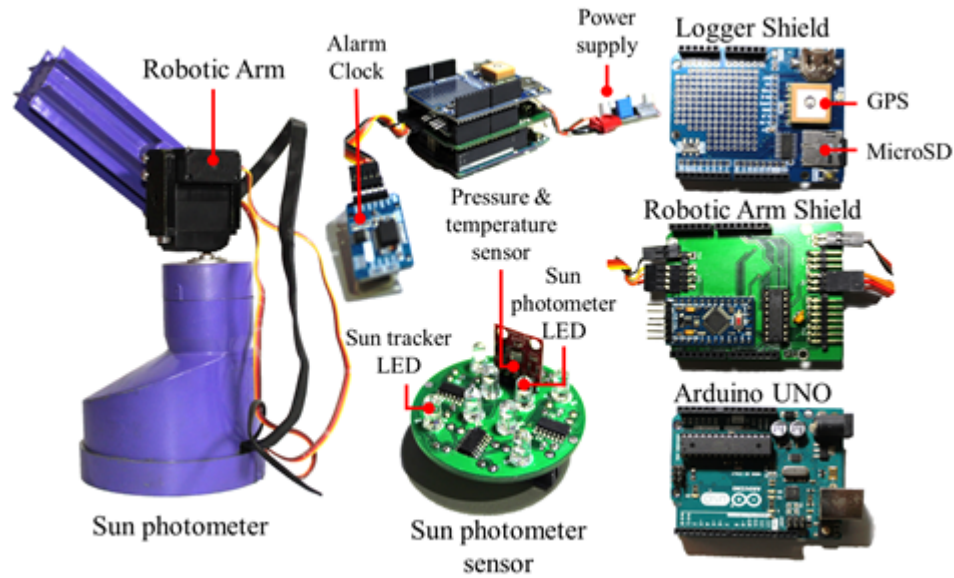
Figure 4.8: Sun Photometer prototype after several instrument improvements.
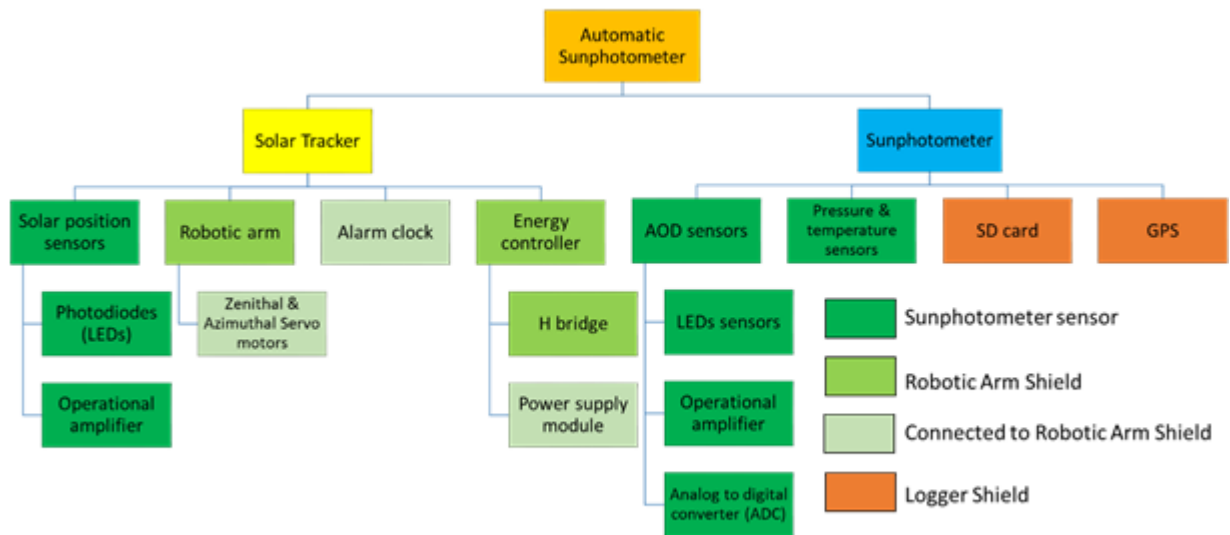
Figure 4.9: Parts of the Sun Photometer prototype. The color shows the location of the component were is each part in the instrument.

4.2.1.   Sun Photometer sensor.

Figure 4.8 presents that although the device has two independent subsystems, in the instrument, some components are placed in the same physical part. In the Sun Photometer sensor, this part includes the AOD sensors and the Sun Tracking sensors. That is because the AOD sensors need to be aligned with the Sun to take proper measurements.

The Sun Photometer sensor from Figure 4.8 could be divided into three components: the Solar position sensor, the AOD Sensor, and the pressure and temperature sensor. This part is connected to the Robotic Arm Shield using a wire.

Solar position sensor

The solar position sensor is used to follow the Sun and align the AOD sensors with it. This component consists of two parts. One of these parts is composed of four LEDs working as photo-detectors, and the other part is composed of a current amplification circuit. The LEDs are regular commercial (unspecified) white LEDs, while the amplifier is an LMC6484 low noise amplifier. In addition, part of the robotic arm is used to cover the sensors when the instrument is not aligned with the Sun. Only when the instrument is aligned, the four sensors receive light from the Sun, working as a quadrant sensor.

AOD sensors

These are the primary sensors of the instrument to measure the AOD. The component consists of four LED sensors working as photo-detectors, the current amplification circuit to amplify the sensors' response, and an Analog to Digital converter (ADC) to convert LED voltages into digital information and send it to the Arduino Uno controller through the robotic arm shield. All the used LEDs correspond to the 408 nm channel used by Toledo et al. (2018) [10], while the amplifier is an LMC6484 low noise amplifier, and the ADC is the MCP3204 12-bit with SPI interface ADC.

Temperature and Pressure

This part is required because the AOD estimation requires measurements of the atmospheric pressure to determine the Rayleigh scattering contribution in the total AOD (see Eq. 3.21) [9]. The temperature is sampled near the AOD sensors. This component uses a BMP180 breakout that measures both variables, connected to the Arduino Uno controller through the robotic arm Shield.

4.2.2. Robotic Arm Shield

This part has two functionalities: (1) Inter-Connect all the components from the robotic arm, the Sun Photometer Sensor, the logger Shield, and the Arduino Uno. (2) Control the Sun tracker subsystem. The Robotic Arm Shield is composed of an Arduino pro mini controller. This micro-controller sets and receives an alarm signal from the RTC clock. It also controls the servo motors and the energy controller, using the Solar position sensor to find the Sun. Figure 4.8 shows the details of this shield.

Robotic Arm

The robotic arm uses two 270º position-controlled servo motors (DSS-M15S). One of them controls the zenithal position, and the other the azimuthal. With these sensors, the movement of the arm can cover more than a hemisphere. 270º servo motors are used because the effective range of servo motors is less than the nominal range (the effective range for a nominal 270º servo motor is only around 240º). Therefore, if 180º servo motors were used,

from example [14], then we will not cover the whole path of the Sun in the sky, specifically during the Summer when the Sun rises from the south-east, then crosses to the north-east, north-west and the sunset occurs in the south-west.

Alarm Clock

This clock triggers (DS3231) an alarm signal every 5 minutes to take a measurement. With that signal, the Arduino pro mini controller leaves the standby mode and estimates the Sun position. If the Sun is visible, the Sun Photometer starts to measure. Otherwise, the instrument comes back to standby mode. The time to take the next measurement is set immediately after the clock signal is received.

Energy controller

The energy controller component energizes the servomotor, the Sun Photometer sensor, the Arduino Uno, and the Logger Shield. This part consists of an H-bridge (SN754410) to control the power supply and a DC-DC converter (LM2596). The converter receives a 12V voltage from the power supply, reducing the voltage to 5V.

4.2.3.   Logger Shield and Arduino Uno Controller.

The logger shield is composed of a GPS receiver and a microSD card module. These components provide GPS time, position, and data storage for the instrument. The Shield is connected to the Arduino Uno that also controls the AOD sensors.

4.3.   Measurement protocol of an instrument.

Measurements are taken following these steps:

1. The alarm clock triggers the alarm signal to the Arduino pro mini controller.
2. The Arduino pro mini controller receives the signal and leaves the standby mode.
3. The Arduino pro mini controller takes the alarm clock hour and sets the next measurement time.
4. The Arduino pro mini estimates a raw Sun position (the base code could be found in [31]). If the Sun appears as visible in the estimation, the Arduino pro mini turns on the servo motors and moves them near the Sun position. In other cases, the Arduino pro mini remains in standby mode.
5. The Arduino pro mini turns on the Arduino Uno controller and the logger shield.
6. The Arduino pro mini starts to find the Sun with the solar position sensors and sends a measurement signal to the Arduino Uno controller.
7. The Arduino Uno controller starts to measure the AOD during 1:30 minutes.
8. After 1:30 minutes, the Arduino pro mini moves the servos to a park position and turns off the tracker. After that, it waits for 1:30 minutes.
9. At the same time, the Arduino Uno controller starts to get the temperature, pressure, height, GPS time, and GPS position. After that, it saves the AOD measurement

together with the time, location, temperature, barometric pressure, and height over the microSD card as a text file.

10. The Arduino pro mini turns off the Arduino Uno and the logger shield, entering on standby mode to waiting for the next measurement.

Respecting to the Sun tracking algorithm, the raw Sun position is used to determine if it is time to take a measure (if the Sun is in the sky) and to move the arm to put the Sun in the Field Of View (FOV) of the Solar sensors (around $30^{\underline{o}}$, if the sensors are outside the FOV the arm could point another bright object). The four Sensors' voltages are compared among themselves to determine the movement vectors to the robotic arm. First, each sensor is compared with the opposite sensor (at $180^{\underline{o}}$ from the sensor), and the directions to move the motors are calculated. Then ,the sum of each sensor response with its two neighbors separately ($+90^{\underline{o}}$ or - $90^{\underline{o}}$ from the sensor) is compared to the opposite group of sensors, and new movement vectors are calculated. Finally, all the movement vectors are added and normalized to move the arm as slowly as possible.

The instrument does not require a precise alignment with the Sun, only needs to be aligned for theoretically 0.00004 seconds, which is when the ADC takes an AOD measurement for all their sensor. Therefore, the robotic arm is always moving around the Sun while the instrument measures.

Another essential feature is that both clocks, the alarm and the GPS, have batteries to save the current time in case the GPS loses contact with the satellite network. As a result, the instrument could work without a GPS connection, and the alarm clock does not lose the hour to calculate the raw position of the Sun or to start the measurement protocol in case of a shutdown of the power source.

4.4. Comparison with Toledo et al. (2018) instrument.

The starting point of the current development was the Sun Photometer developed by Toledo et al. (2018), from now Sun Photometer V2 [10]. Table 4.2 summarizes the differences between the Sun Photometer V2 and our instrument (now on Sun Photometer V3).

The Sun Photometer V3 improves the Sun Photometer V2 capabilities. The only exception is the number of wavelengths available. The reason for that is easier to use the 408 nm sensor to test the prototype. Furthermore, the Sun Photometer V3 is an automatic instrument, while the V2 is user-dependent. The automation not only implies a more effortless field operation, but it is also critical for the calibration procedure. The statistics, associated with the number of days for the pre- and post-campaign calibration, are fundamental for the measurements' precision. Nevertheless, the V3 cost of materials is only 47% more expensive than the V2 Sun Photometer. Table 4.3 shows the detail of the cost of materials for the V3 Sun Photometer.

4.5. Measurement procedure

The measurement procedure considers the following steps proposed by Toledano et al. (2018): (1) Calibrate the instrument. (2) Take the measurements on the site. (3) Re-

Prototype	Sun photometer V2	Sun photometer V3
Number of Channels	2	4
Wavelength Available	408 / 562 nm	408 nm
OPAMP	TLC272	LMC6484
ADC	10 bits	12 bits
Sample rate	9.615 kHz (2x 4.807 kHz)	100 kHz (4x25kHz)
Clock	DS1307	DS3231 + GPS
Storage	μSD Card	μSD Card
Custom Characteristics	User Interface	Automatic Sun-tracker
Cost of Materials	$\sim$ 150 USD	$\sim$ 220 USD

Table 4.2: Comparison between V2 and V3 Sun photometers prototypes.

Component	Cost (US)	Units	Total Cost (US)
Arduino UNO	22	1	22
Arduino pro mini	9.95	1	9.95
PCB Sun Photometer Sensor	5	0.2	1
PCB Robotic Arm Shield	5	0.2	1
LEDs	0.5	8	4
Amplifier LMC6484	3.88	2	7.76
ADC MCP3204	4.06	1	4.06
Electronics Components	10	1	10
Pin Headers	10	1	10
Cables	10	1	10
Case	10	1	10
Logger Shield	49.95	1	49.95
Servo Motor 270$^{\mathrm{o}}$	14.9	2	29.8
SD Card	9.95	1	9.95
Power Supply	12	1	12
BMP180	9.95	1	9.95
DS3231 RTC Clock	17.5	1	17.5
Total			218.92

Table 4.3: Cost of Materials for the V3 Sun Photometer

calibrate to check the measurements. Figure 4.10 presents an image of the Sun Photometers calibration procedure. The instruments taking measures to calibrate them.

Figure 4.10: Version 3 Sun Photometers measuring for Calibration.

4.5.1. Langley plot procedure

The calibration is required to determine the extraterrestrial monochromatic intensity I_0 at the AOD sensor's wavelength. To do that, Beer-Lambert-Bouguer's Law exhibits two dependencies for the received monochromatic intensity: The OD and the air mass. The Langley calibration method requires a stable OD place. For example, the top of a mountain, where there are not aerosols emissions and less variation of abortion gases at the relevant wavelength. Under those conditions, the intensity only depends on the air mass and light path through the atmosphere. Therefore, if we take measurements for different Sun positions (different air mass values), we can extrapolate the irradiance when the air mass is zero. That procedure is known as Langley calibration.

Applying logarithm and accommodating the terms in Eq. 3.19 (the Beer-Lambert-Bouguer's Law), results Eq. 4.1. The instrument measures voltages, which are proportional to the monochromatic irradiance. Therefore, replacing the irradiances by their proportional voltages values and reorganizing, Eq. 4.2 displays the Langley plot calibration formula. If the airmass m is considered as an independent variable and $ln(V_i)$ as the dependent variable, then the result is a linear equation, with slope τ_λ (the OD) and intersection $ln(V_0)$. V_0 is called the Langley constant. Thus, plotting $ln(V_i)(m)$ it is possible to determine $ln(V_0)$ under constant τ_λ, completing the Langley calibration.

$$ln(I_\lambda) = ln(\frac{I_{\lambda\infty}}{r^2}) - \tau_\lambda m, \tag{4.1}$$

$$I_\lambda \quad \alpha \quad V_i,$$

$$I_{\lambda\infty} \quad \alpha \quad V_0,$$

$$ln(V_{\mathrm{i}}) = ln(\frac{V_0}{r^2}) - \tau_\lambda m. \tag{4.2}$$

The main advantage of this method is simplicity. However, a proper place is required to perform it. Usually, these places are far from cities or towns. Furthermore, we need optimal weather conditions and several sunny days to properly characterize the extraterrestrial intensity (or Langley constant, for calibration purposes). Moreover, if several instruments are considered for that kind of calibration, then the logistic problems could be relevant. Some improvements to this method have been proposed. Some examples could be found in [1] and [20].

Langley calibration was performed for one of our instruments. Figure 5.1 shows the results. Notice that the air mass profile was taken when the Sun was declining. To calculate the air mass, we use eq. 4.3 proposed in Brooks et al. (2001), where z is the zenithal angle, and to calculate the solar position for analysis purposes, we use the NREL algorithm proposed by Reda et al. (2004) [32].

$$m = \frac{1.002432cos^2(z) + 0.148386cos(z) + 0.0096467}{cos^3(z) + 0.149864cos^2 + 0.000303978} \tag{4.3}$$

4.5.2. Parameter fitting with Cimel measurements

An alternative method to calibrate a Sun Photometer is to compare its measures with another calibrated instrument. In this case, the measurements are compared with a NASA calibrated instrument: A Cimel Sun Photometer. A difficulty of that is the wavelengths are not the same for both instruments. For that reason, the Ångström exponent extrapolation [33] is required. This exponent relates different AOD at different wavelengths using Eq. 4.4.

$$\tau(\lambda) = \tau_1\lambda^{-\alpha} \tag{4.4}$$

$$ln(\tau(\lambda)) = ln(\tau_1) - \alpha ln(\lambda)$$

Where τ_1 in the AOD at 1 μm and α is the Ångström's exponent. If Eq. 4.4 is evaluated for two AOD at wavelength λ_1 and λ_2, then the equation can be used to obtain Eq. 4.5. To determine the Ångström's exponent at the wavelength of the Sun Photometer V3 as presented in Eq. 4.6

$$\frac{\tau_{\lambda 1}}{\tau_{\lambda 2}} = (\frac{\lambda_1}{\lambda_2})^{-\alpha} \tag{4.5}$$

$$\tau_{\lambda 3} = \tau_{\lambda 2}(\frac{\lambda_3}{\lambda_2})^{-\alpha} \tag{4.6}$$

Another property of the Ångström exponent is related to the particle size distribution [3]: On one hand, if $\alpha \geq 1$, then the coarse mode dominates the size of the aerosol distribution. On the other hand, if $\alpha \geq 2$, then the fine mode dominates the distribution.

The Cimel Sun Photometer measure in several wavelengths. It is possible to estimate the AOD values at ~ 408 nm near the equivalent wavelength for our LED-based AOD sensors. Toledo et al. (2018) show no significant difference between estimate the AOD using the equivalent wavelength or the whole spectral wide sensor response. Suppose we take several measures together with the Sun Photometer v3 and a Cimel Sun Photometer. In that case, the error between both measurements could be minimized using as variables the extra-terrestrial voltage V_0 (proportional to the extra-terrestrial irradiance) and the wavelength λ. In this case, the mean error among the ground truth instrument, the Cimel Sun Photometer, and our prototype is known as Root Mean Square Error (RMSE).

Definition 4.1 *Root Mean Square Error (RMSE)*

$$RMSE = \sqrt{\frac{\Sigma_{i=1}^{i=n}\left(\tau_{\lambda i}(\lambda) - \tau_i(\lambda, V_0)\right)^2}{n}}$$

Where n is the number of measurements taken, V_0 is the voltage associated to extra-terrestrial irradiance, $\tau_{\lambda i}(\lambda)$ the estimated AOD measurement at wavelength λ from the Cimel Sun Photometer at the measurement i, while $\tau_i(\lambda, V_0)$ is the estimate AOD measurement for the prototype given V_0 and λ taken at the same time that $\tau_{\lambda i}(\lambda)$.

Eq. 4.7 shows the RMSE as an optimization problem. This approach allows us to determine the calibration Langley constant and the equivalent wavelength without a Langley calibration without knowing the AOD sensor response. The only consideration is that there can not be Optical Depth due to the gases in the response's spectra, such as in the case of our AOD sensor.

$$\min_{ln(V_0),\lambda} \sqrt{\frac{\Sigma_{i=1}^{i=n}\left(\tau_{\lambda i}(\lambda) - \frac{ln(V_0)-ln(V_i)-\tau_R\frac{p_i}{p_0}m_i}{m_i}\right)^2}{n}} \tag{4.7}$$

In Eq. 4.7 n is the number of measurements taken, V_i is the voltage measured in the measurement i, V_0 is the voltage associated to extra-terrestrial irradiance, and $\tau_{\lambda i}(\lambda)$ the estimated AOD measurement at wavelength λ from the CIMEL Sun Photometer at the measurement i.

The Eq. 4.7 is an optimization problem, where the Langley constant value V_0, and the equivalent wavelength λ are the parameters to fit, minimizing the distance among the Cimel measurements and the V3 instruments. In the Results section, we show a comparison between the Langley plot method and the parameter fitting method.

4.6. Measurement campaigns

The calibration of the instruments is required to take comparable measures. However, to perform a distributed campaign with several devices, additional stages are needed. Figure 4.11 demonstrates the proposed methodology for a city-scale campaign with the instruments.
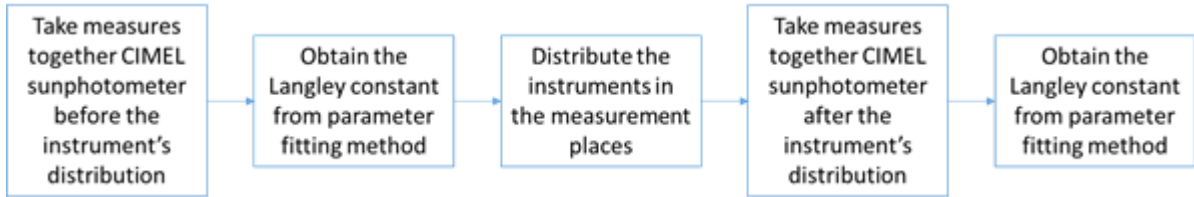
Figure 4.11: Schematic of the procedure of Sun Photometers' calibration.

Figure 4.11 tells us that the city-scale campaign procedure works with a methodology that requires calibrations before and after the campaign. This procedure is to ensure that the instruments have not changed significantly during the campaign. Furthermore, to know if there are some damages to the prototypes. Alternatively, one can make the calibration before and after, not only to check. In the discussion section, the calibration is studied intensely, and improvements are proposed.

Finally, Figure 4.12 shows the sites chosen to take measures at the city-scale. The aim was to have several stations distributed in the city and observe how the AOD changes in each place with time. The goal of this kind of campaign is to demonstrate the feasibility and the need for a Sun Photometer network to explore the dynamic behavior of aerosols over a city area.
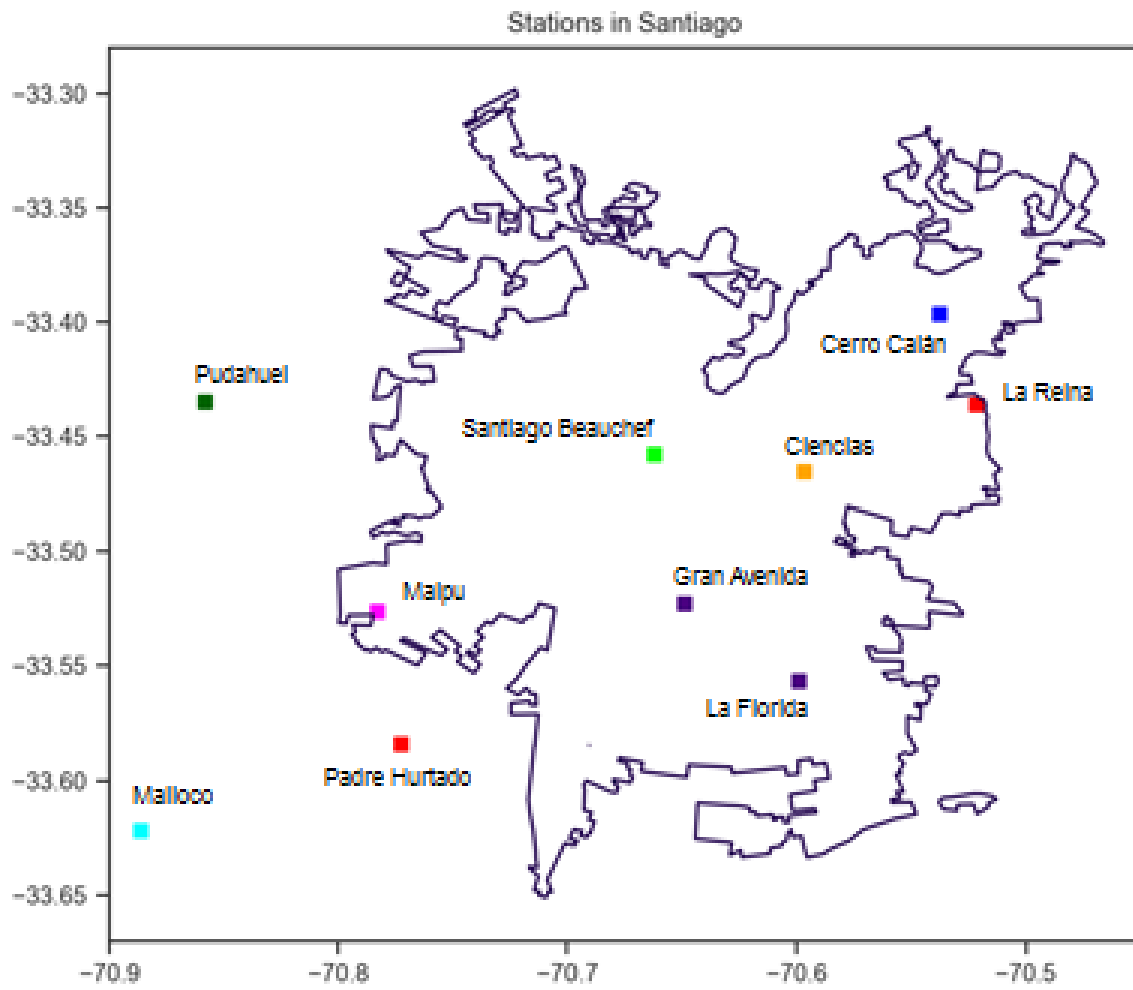
Figure 4.12: All the planned city stations for the distribute measurements' campaign.

Chapter 5

Results

Some of the most important findings of this work are summarized: First, data related to the calibration process is presented to compare the Langley plot calibration and the proposed Parameter fitting calibration. Second, the error of the measures of the developed instruments is determined. Finally, the results of the city-scale campaign are exhibited.

5.1. Langley plot and Calibration Results Comparison.

The Langley constant obtained by the Langley plot calibration and the parameter fitting proposed method is compared. Figure 5.1 exhibits the Langley plot performed on May 18, 2018. The test was performed in Valle Nevado, 65 kilometers east of Santiago de Chile, around 3000 m.a.s.l. How it was explained in the Langley Plot calibration section in the previous chapter, the place to perform this procedure must require a stable aerosols level during the day. This campaign's objective was to assure if the instrument can measure automatically because the place is not the most adequate to perform a Langley calibration (as is presented in the results of Toledo et al. (2018)). However, the measurements are good enough to estimate a Langley constant. The measurements were taken between 18:13 and 19:58 UTC, and the zeniths' angles are between 57.71^{o} and 71.4^{o}. The used air masses are between 1.5 and 4, which are the same ranges used by Toledo et al. (2018).

The other method used is the parameter fitting method. In this method, our instrument measures with a reference instrument: the Cimel Sun Photometer, and it is not necessary a site with the requirements of a Langley Plot calibration, only that the reference instrument is calibrated. Then, the parameters of the model are adjusted to minimize the RMSE between both devices. Eq. 4.7 exhibits that two parameters need to be adjusted: the wavelength and the Langley constant. The former is to estimate the RS, while the latter is the searched parameter in the Langley Plot calibration. Table 5.1 displays the difference between the Langley Constant obtained by the methods, while 5.2 demonstrates the difference of the RS obtained by the parameter fitting method and the estimation made from Toledo et al. (2018) [10] for the same sensor.

Toledo et al. (2018) use the same sensor, and it has a mean response wavelength of 408
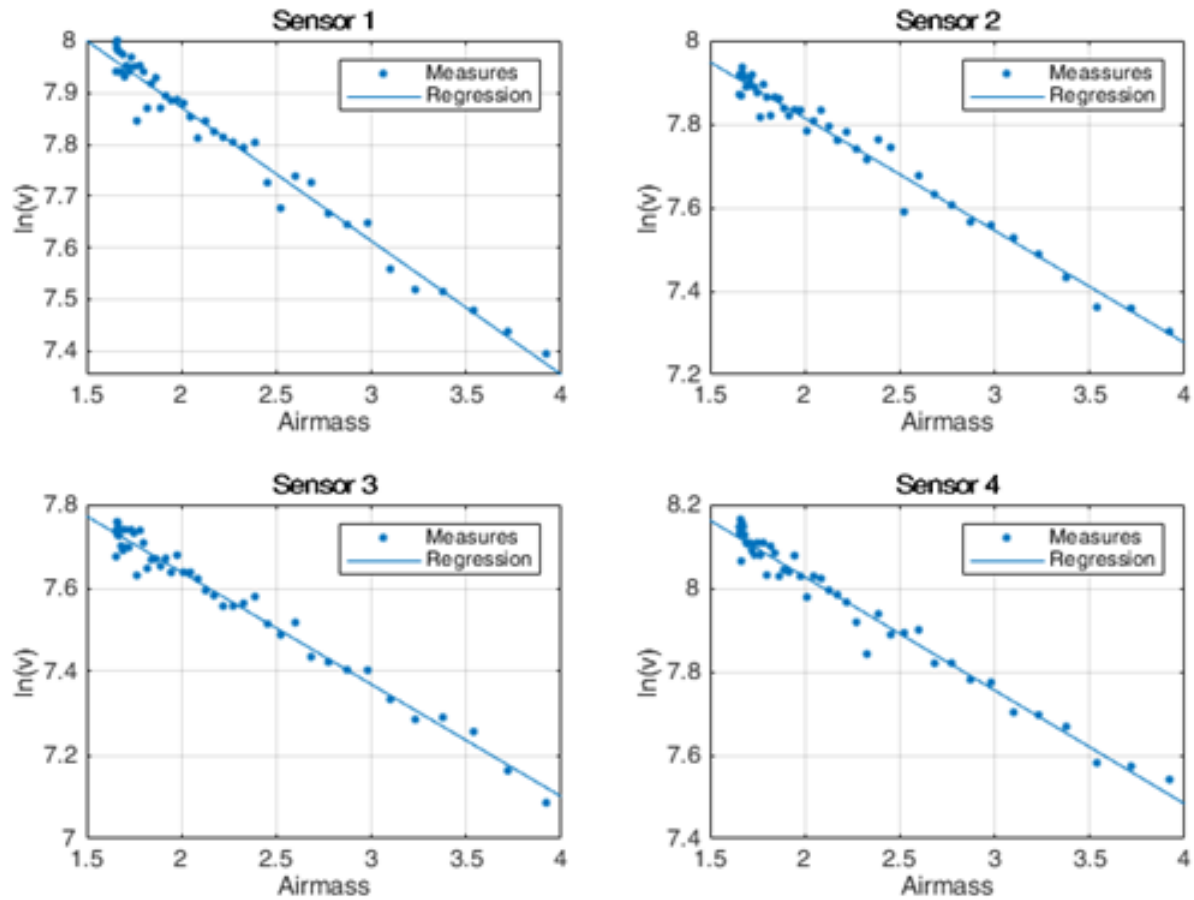
Figure 5.1: Langley plot from Valle Nevado (3.000 m.a.s.l.)

Sensor Number	Langley Constant (Langley Method)	Langley Constant (fitting model)	Absolute Error	Relative error
Sensor 1	8.39	8.32	-0.07	-0.83%
Sensor 2	8.35	8.32	-0.03	-0.36%
Sensor 3	8.18	7.90	-0.28	-3.42%
Sensor 4	8.57	8.59	0.02	0.23%
All sensors	8.37 ± 0.16	8.28 ± 0.29	-0.09 ± 0.13	-1.10% ± 1.61 %

Table 5.1: Results of a Langley constant for both methods.

nm. However, from Table 5.1, the parameter fitting method determines a wavelength that differs from ± 8 nm, respecting the mean value found for the same kind of LED by Toledo et al. (2018). That implies a difference of 0.03 in the RS estimation, respecting the same difference.

The results of Tables 5.1 and 5.2 show a mean difference of 1.1% and a standard deviation of 1.61 % among sensors. Those differences are reasonable considering the Langley plot calibration conditions and because both were performed only once. On the other hand, the RS's differences are reasonable, considering the low difference wavelength estimation.

Sensor Number Number	Rayleigh Constant (Mean [10])	Rayleigh Constant (fitting model)	Absolute Error	Relative error
Sensor 1	0.33	0.30	-0.03	-8.86%
Sensor 2	0.33	0.32	-0.01	-2.79%
Sensor 3	0.33	0.34	0.01	3.29%
Sensor 4	0.33	0.36	0.03	9.36%
All sensors	0.33 ± 0.00	0.33 ± 0.03	-0.00 ± 0.03	$0.25\% \pm 7.84\%$

Table 5.2: Rayleigh scattering obtained by the parameter fitting sensor and the reported for Toledo et al. 2018 blue sensors (408 nm).

Figure 5.1 and Tables 5.1 and 5.2 demonstrate that the prototype can measure and the parameter fitting procedure is a valid calibration option compared with the Langley plot calibration. This procedure's main advantage is that it could be performed everywhere, while a pattern instrument exists instead of the Langley plot, where a minimal variation of aerosols is required in the measurement site. This approach is valuable in a city-scale setting because all instruments are calibrated using the same ground truth instrument. In contrast, all systematic errors of the patter instrument are transferred to the prototype instruments.

5.2. Measurement's errors characterization.

To study and compare measurements differences of the instruments, two error sources that need to be estimated:

- The difference of the measurements compared to the Cimel AERONET Sun Photometer estimation.
- The consistency among all our instruments.

In the following, the procedure to estimate both errors is explained, and the results are presented. In the discussion section, the errors of the instruments respect the Cimel Sun Photometer are compared and discussed.

5.2.1. Measurement errors compared with Cimel.

Our instruments have been measuring together with Cimel for several hours and different days to estimate this error. Then, the measures can be compared. Figure 5.2 shows and a scatterplot of the Cimel and one of our sensors. In this Figure, the equivalent Cimel measurement for our instrument wavelength (408 nm) was used.

Table 5.3 summarizes the standard deviation and mean differences between the Cimel Sun Photometer and each of all our sensors.

The results from Table 5.3 indicate an average difference under the significance level, while the standard deviation is similar to the reported error from Cimel Sun Photometer [4]. In the discussion section, we discuss this number and the implications of developing a city-scale network.
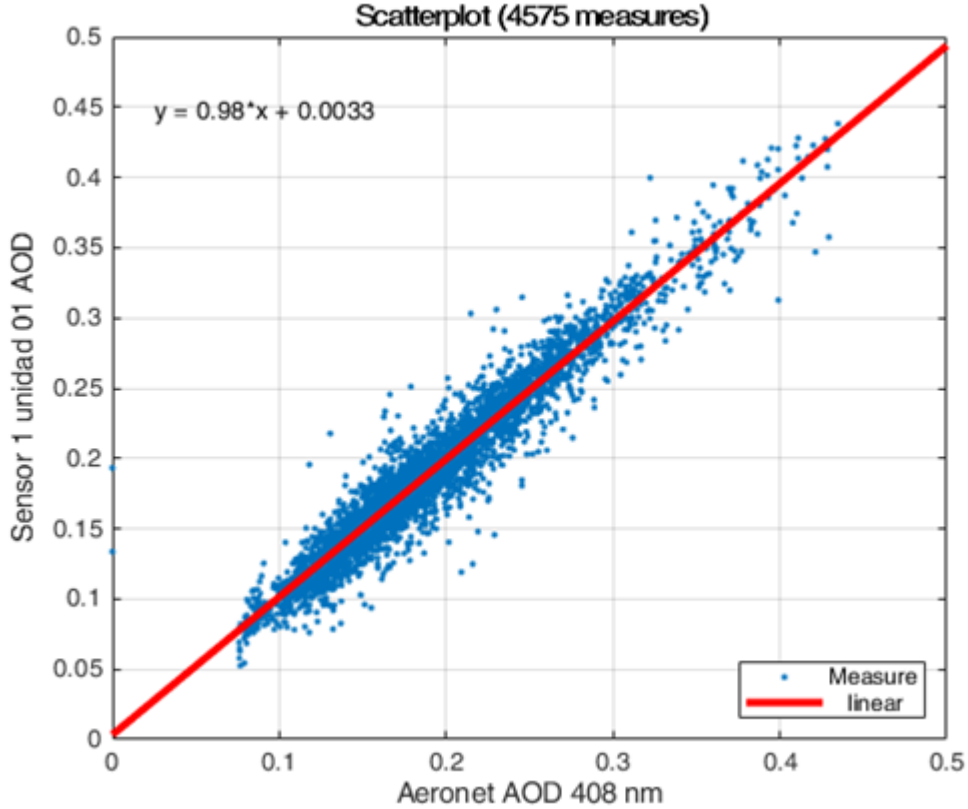
Figure 5.2: Scatter plot between sensor 1 of our unit 1 and the Cimel AERONET measurements (over 4,000 measurements).

5.2.2. Consistency among all our instruments.

This section aims to compare the measures only using our prototype instruments. For this test, the prototypes and the pattern instruments measure together in the same place for a whole day. We compare all the measurements for the different prototype instruments and sensors and estimate each time of measurement a mean and a standard deviation with the calibration constants. That result gave us an estimation of the instrument measurement error.

For this estimation, we consider two cases: Using the same measurements to calibrate the instrument with Cimel, and then compare among all the instruments, and separating the calibration measurements from the comparison measurements. Figure 5.3 shows a plot of the standard deviation for a day of measures, while Figure 5.4 presents the measures compared with Cimel estimation for the same wavelength. In this case, we use the same data to calibrate the instruments. On the other side, Figure 5.5 and 5.6 shows the same information that Figures 5.3 and 5.4, the only difference is that the instruments were calibrated with measures taken the day before. This consideration is because to figure out if there is some over-fitting in the calibration parameters.

Finally, Table 5.4 displays the mean bias of all the instruments with the Cimel Sun Photometer for all the measures of the day. Table 5.5 exhibits the average standard deviation

Unit and Sensors	Number of Measures	Average Difference	Standard Deviation
Unit 1, Sensor 1	4575	-0.0003	0.016
Unit 1, Sensor 2	4641	-0.0009	0.021
Unit 1, Sensor 3	4093	-0.0004	0.036
Unit 1, Sensor 4	3362	0.0040	0.043
Unit 2, Sensor 1	1532	-0.0011	0.019
Unit 2, Sensor 2	1336	-0.0034	0.013
Unit 2, Sensor 3	1561	-0.0009	0.016
Unit 2, Sensor 4	1195	-0.0007	0.023
Unit 3, Sensor 1	-	-	-
Unit 3, Sensor 2	1371	0.0001	0.013
Unit 3, Sensor 3	1381	0.0012	0.013
Unit 3, Sensor 4	1345	0.0017	0.013
Unit 4, Sensor 1	1051	0.0003	0.011
Unit 4, Sensor 2	610	-0.0015	0.013
Unit 4, Sensor 3	541	0.0022	0.045
Unit 4, Sensor 4	524	-0.0004	0.010
Unit 5, Sensor 1	1229	-0.0022	0.068
Unit 5, Sensor 2	1258	-0.0020	0.026
Unit 5, Sensor 3	1839	0.0001	0.039
Unit 5, Sensor 4	-	-	-
Unit 6, Sensor 1	567	-0.0001	0.028
Unit 6, Sensor 2	569	-0.0003	0.015
Unit 6, Sensor 3	902	0.0011	0.032
Unit 6, Sensor 4	1217	0.0013	0.014
Unit 7, Sensor 1	1087	-0.0031	0.050
Unit 7, Sensor 2	1240	-0.0021	0.033
Unit 7, Sensor 3	1365	0.0018	0.017
Unit 7, Sensor 4	1309	0.0016	0.012
Unit 8, Sensor 1	1367	-0.0004	0.011
Unit 8, Sensor 2	1410	-0.0007	0.016
Unit 8, Sensor 3	1352	0.0018	0.013
Unit 8, Sensor 4	1340	-0.0009	0.011
Unit 9, Sensor 1	692	0.0024	0.013
Unit 9, Sensor 2	602	0.0002	0.012
Unit 9, Sensor 3	709	0.0032	0.010
Unit 9, Sensor 4	599	0.0022	0.011
Unit 10, Sensor 1	309	0.001	0.012
Unit 10, Sensor 2	305	-0.0026	0.013
Unit 10, Sensor 3	214	0.0027	0.019
Unit 10, Sensor 4	309	0.0026	0.015
Average	1340	0.0002	0.021

Table 5.3: Average difference and standard deviation between Cimel and each sensor.
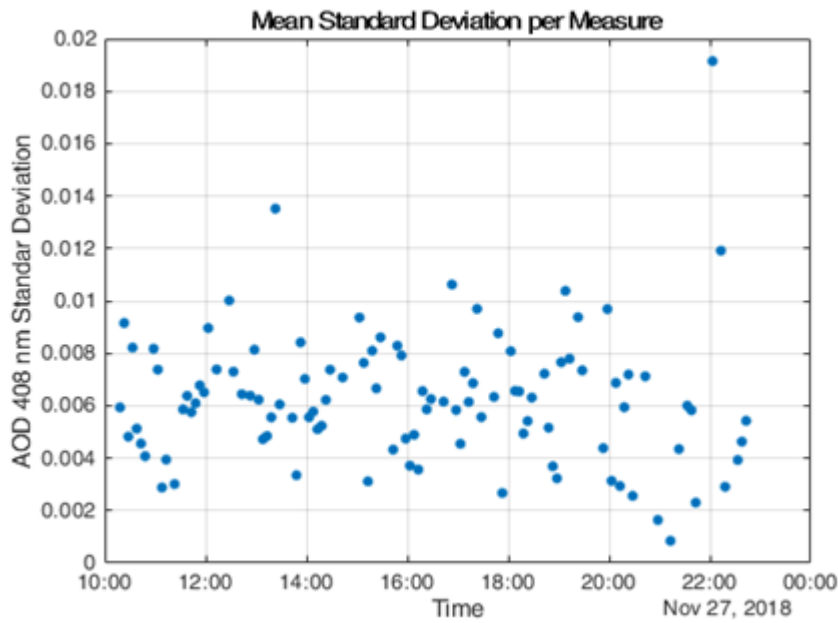
Figure 5.3: Standard deviation for measures of different instruments. We use the same measures to calibrate the instrument.
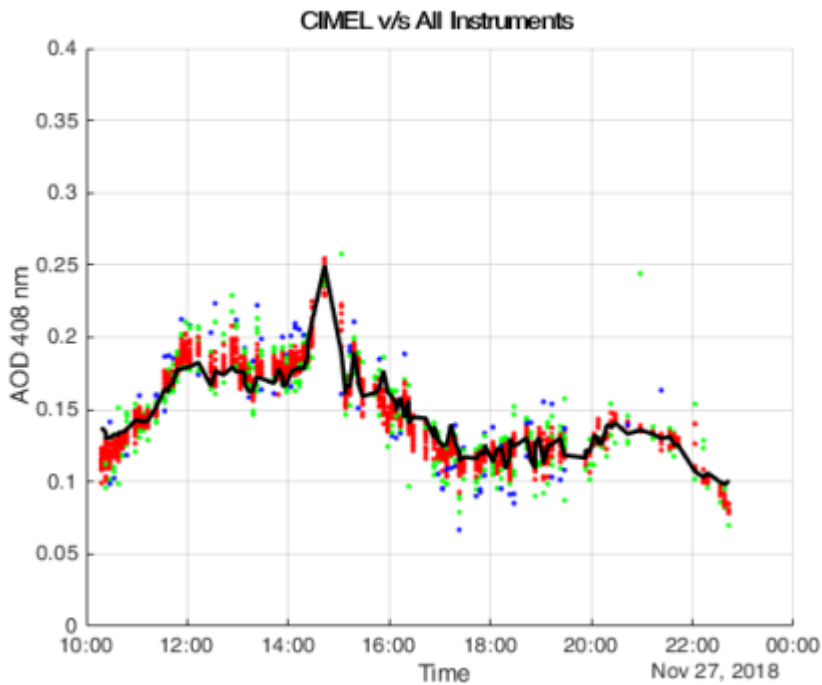
Figure 5.4: Comparison among our instruments measures (Red points: One standard deviation, Green points: two standard deviations, and Blue points: three standard deviations) and the Cimel estimation (Black line). We use the same measures to calibrate the instrument.

among all our instruments considering all the measurements from the day. In both Tables, the cases using the same measures to calibrate and using different data to calibrate are considered.

46
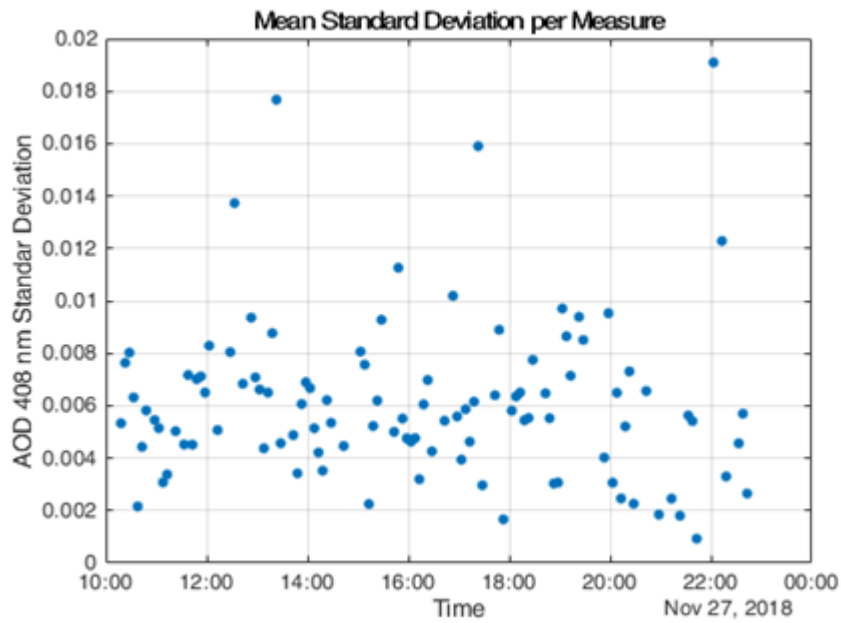
Figure 5.5: Standard deviation for measures of different instruments. We use the measures from the previous day to calibrate the instrument.
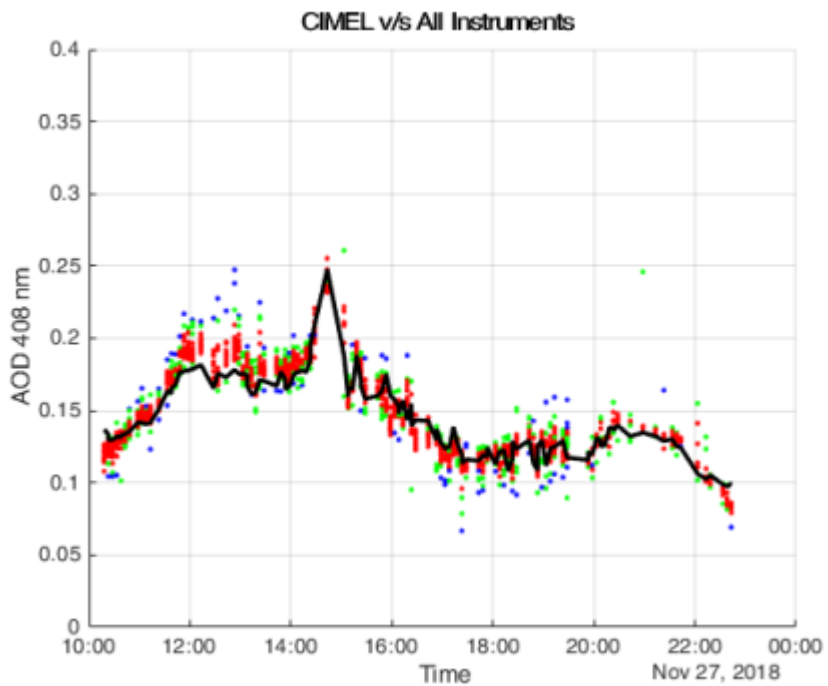
Figure 5.6: Comparison among our instruments measures (Red points: One standard deviation, Green points: two standard deviations, and Blue points: three standard deviations) and the Cimel estimation (Black line). We use the measures from the previous day to calibrate the instrument.

Those results reveal a standard deviation under 0.02 for all measurements simultaneously, while the mean bias compared with Cimel is negligible compared with the error level consid-

Bias Cimel v/s All Instruments (Calibration)	Bias Cimel v/s All Instruments (Independent)
0.0008	-0.0017

Table 5.4: Mean bias of all our instruments and the Cimel Sun Photometer.

Mean Standard Deviation All Instruments (Calibration)	Mean Standard Deviation All Instruments (Independent)
0.006	0.006

Table 5.5: Mean standard deviation considering all our instruments.

ered by the standard deviation. In the discussion section, those results are interpreted.

5.3. Measurement Campaigns.

The measurement campaign consists of positioning the instruments in different places and measure at the same time. Depending on the availability of the devices, the number of stations varies from 2 to 6. All the AOD times series obtained are compared with the AERONET Santiago Beauchef station, considered the ground truth for all cases. Some time series are incomplete, considering the availability and obstacles of the stations. The main problems are obstacles between the Sun and the instrument and also some technical issues.

The following Figures exhibit the results of the measurements for seven days. Those results are relevant because they reveal AOD displacements or different behaviors for different stations. Both cases are impossible to detect using the available instruments or methods to measure AOD. In addition, satellite pictures are provided in each figure to check if there are some clouds during the measurement time.

Figure 5.7 displays a different behavior between La Florida and La Reina station. While the latter follows the rise of AOD like AERONET station. In the former, the AOD decrease during the afternoon. Both stations are around 12.5 Km from Beauchef station. That reveals a different behavior of aerosols, depending on the place of the city.

Figure 5.8 reveals an increase of AOD in the Beauchef station during the afternoon (We also have one of our instruments measuring together). Then, a rise with similar characteristics appears sequentially in Ciencias station and Cerro Calán station, exhibiting a displacement of the surge of AOD through the city.

Figure 5.9 the displacement moves in the opposite direction of Figure 5.8. Unfortunately, Ciencias Station did not have availability for the whole day. However, the moments of availability presents an increase of AOD before AERONET, but after Cerro Calán station. The only difference during this day was a wildfire in the region, as shown in the afternoon image (from Aqua satellite) in the Figure. It seems that aerosols' emission on the east side of the city could influence the behavior of the AOD in the city.

Figures 5.10 and 5.11 do not display a relevant variation, only a more considerable amount of AOD than AERONET during the morning in the southwest stations (Malloco, Padre

Hurtado, and Gran Avenida) and a shorter AOD in the northeast station (Cerro Calán). In the afternoon, the AOD measurements of all the stations are similar.

Figure 5.12 shows a rise of AOD that starts in the Padre Hurtado station (note that the surge does not appear in the Malloco station on the west). Later, it seems to move sequentially to Maipu, Gran Avenida, and Beauchef (AERONET). In the afternoon, there is a rise in the AOD in the Cerro Calán station in the northeast.

Finally, Figure 5.13 adds a station in Pudahuel in the North West. This day shows that all the stations around the city (Malloco, Padre Hurtado, and Pudahuel) have lower levels of AOD during the whole day than inside the city stations. It looks like the emission or displacements of aerosols occur inside the city that day.

The cases presented have demonstrated a Sun Photometer network's capability to study the dynamic of aerosols and AOD in an urban area as Santiago. With several low-cost prototypes, the variability of the AOD in the city was revealed. With the actual available instruments and budgets could be impossible to show that. The results also demonstrate the advantages and possible capabilities of a city-scale Sun Photometer network, and the complete procedure exhibits the feasibility of this approach.

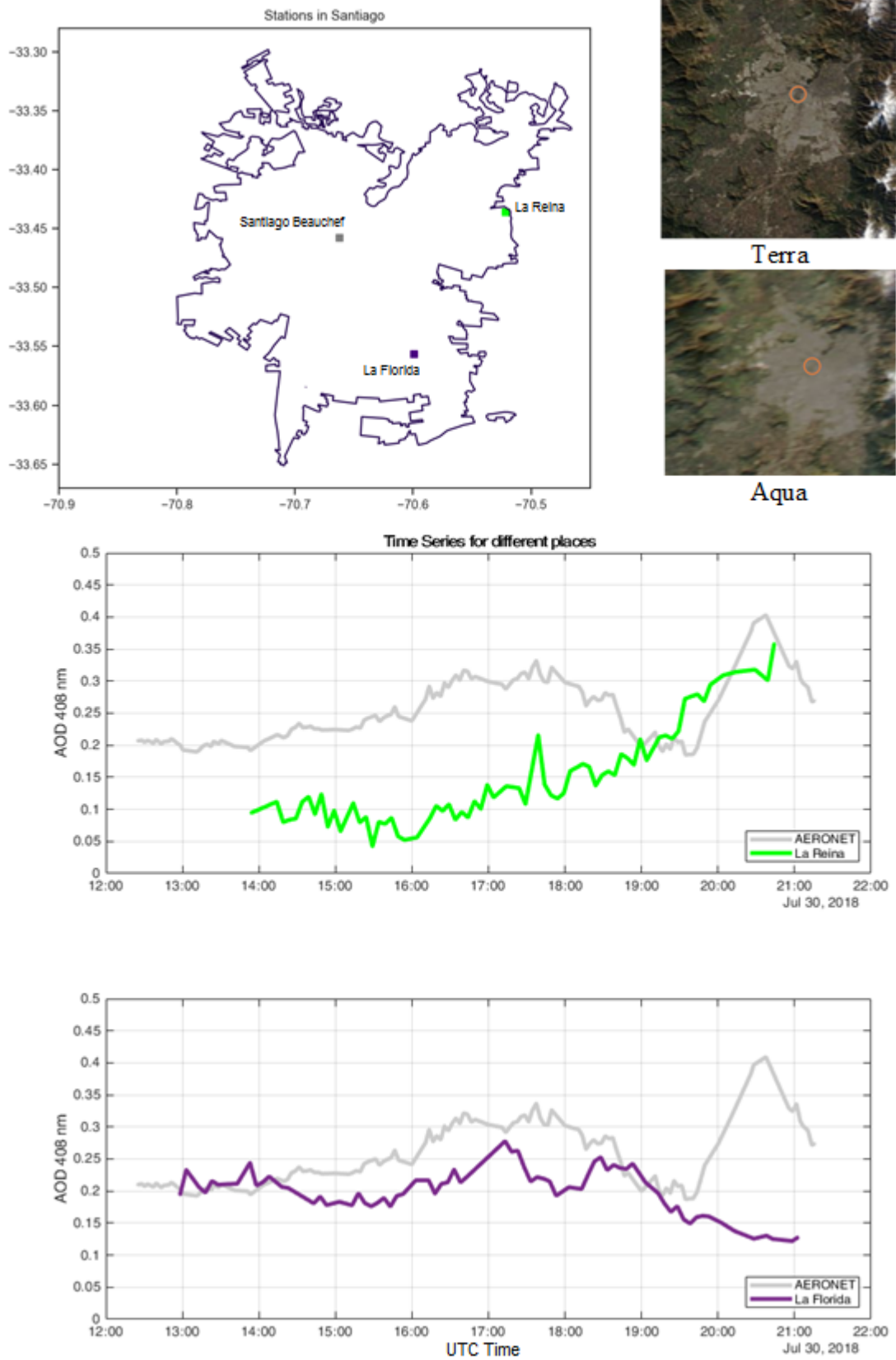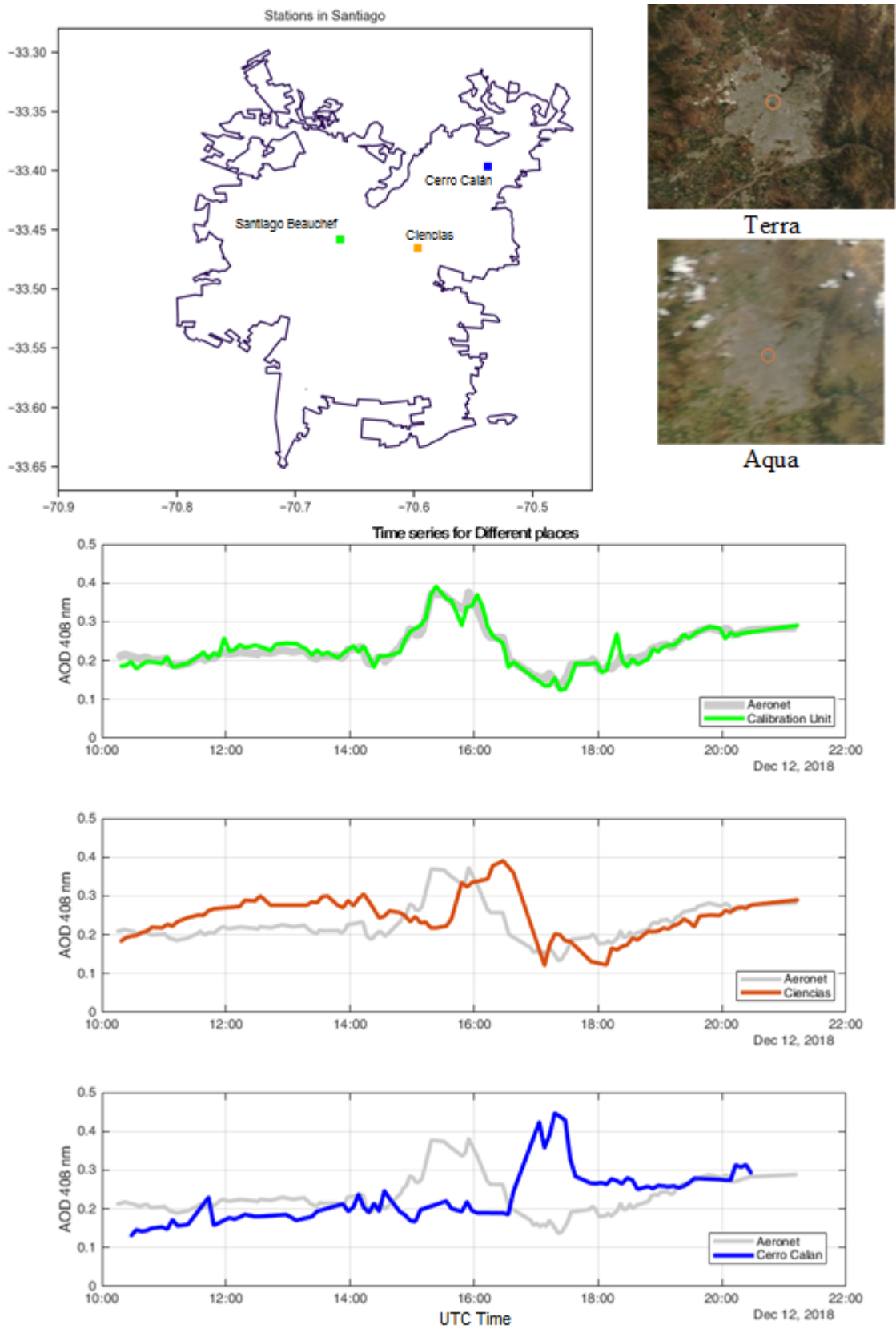Figure 5.7: City-scale measurements For July 30, 2018.

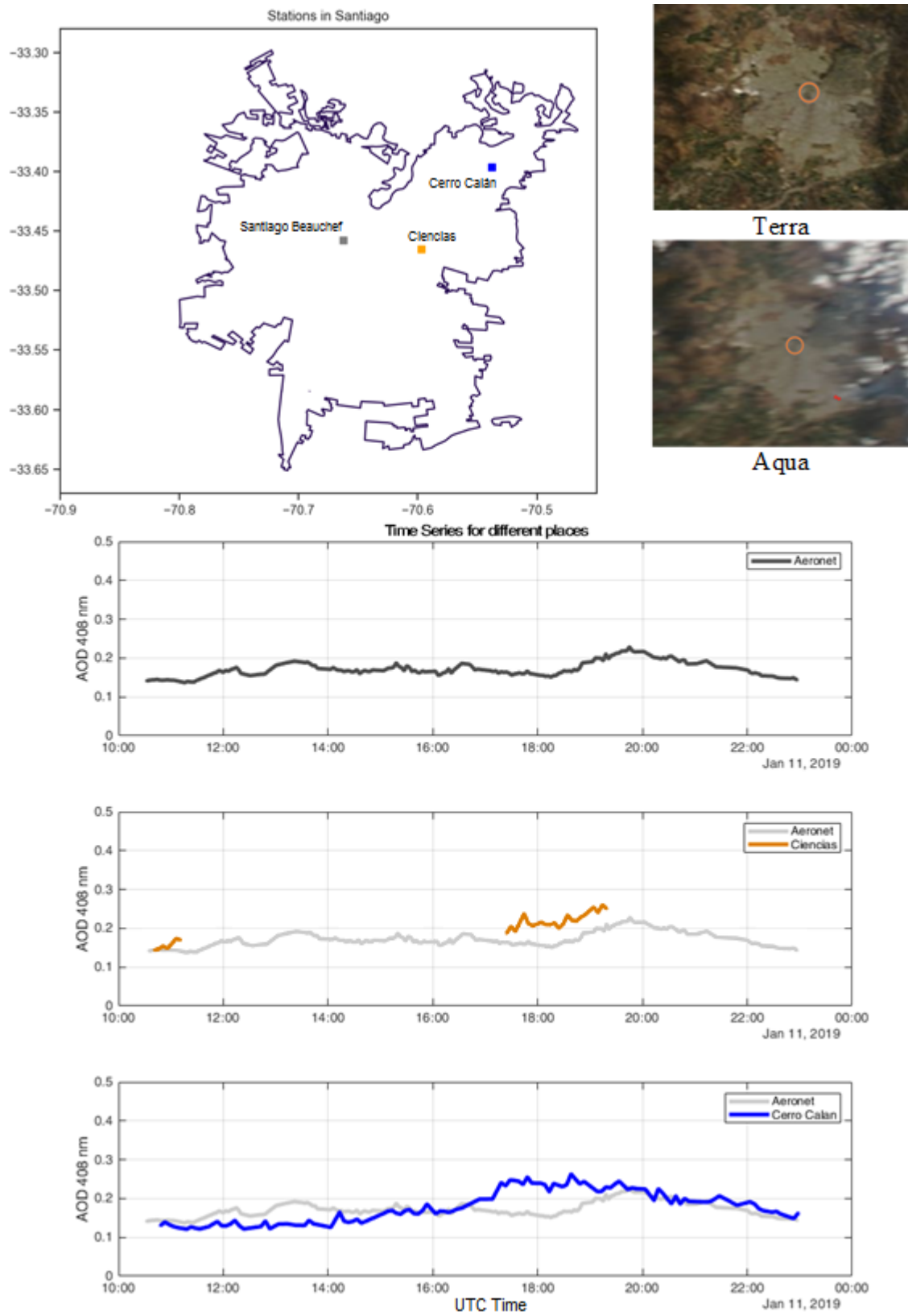Figure 5.8: City-scale measurements for December 12, 2018.

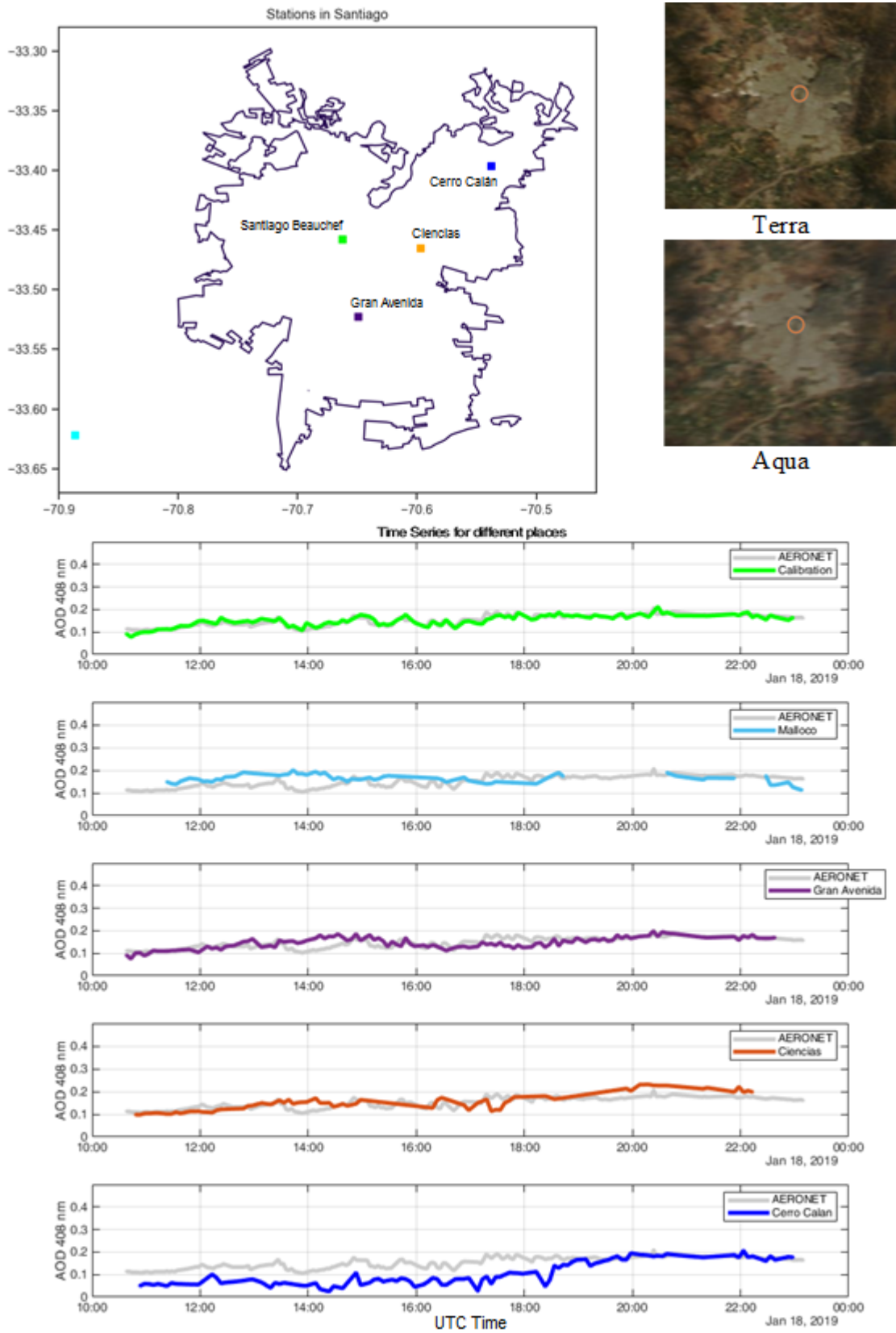Figure 5.9: City-scale measurements for January 11, 2019.

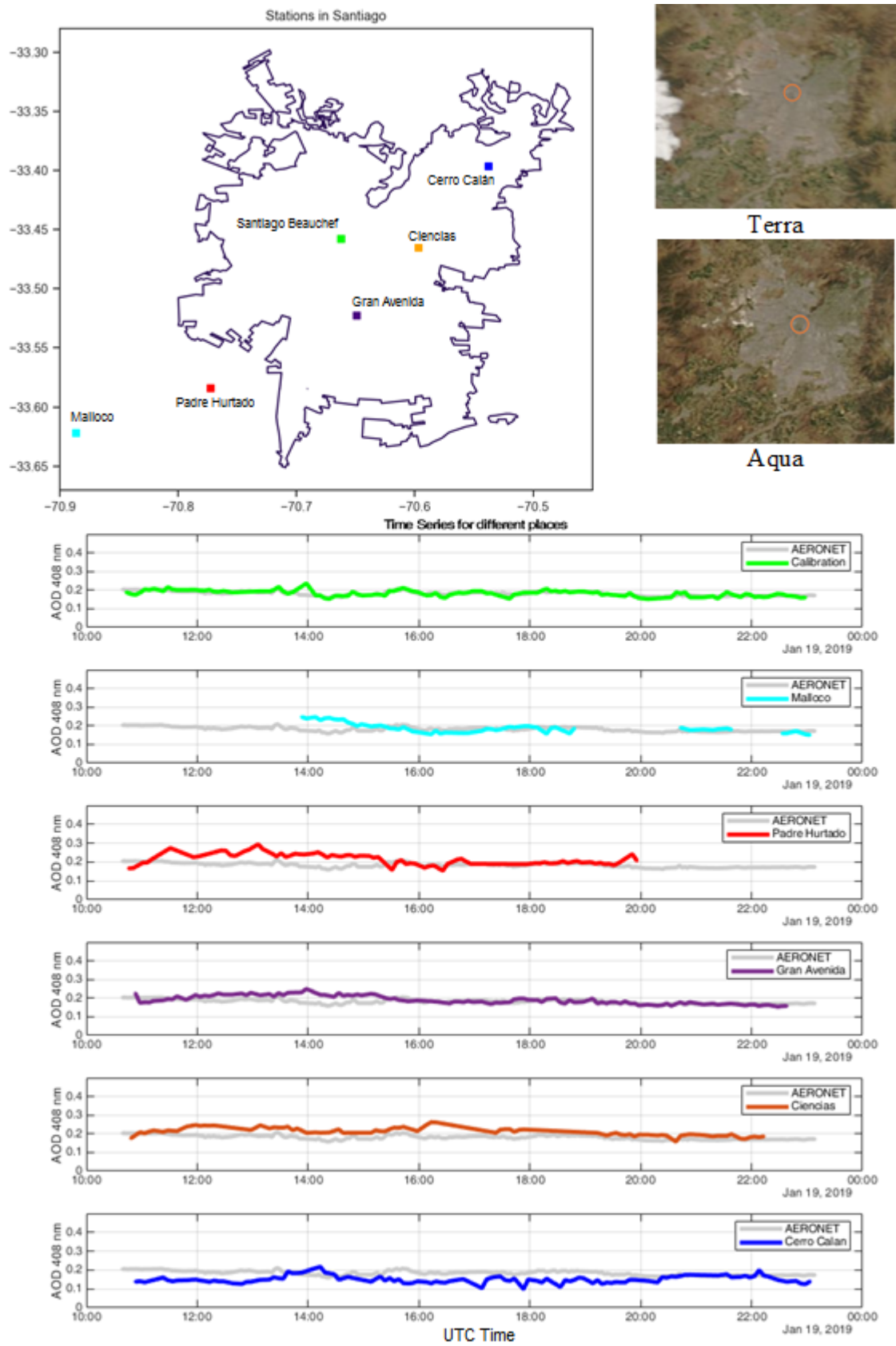Figure 5.10: City-scale measurements for January 18, 2019.

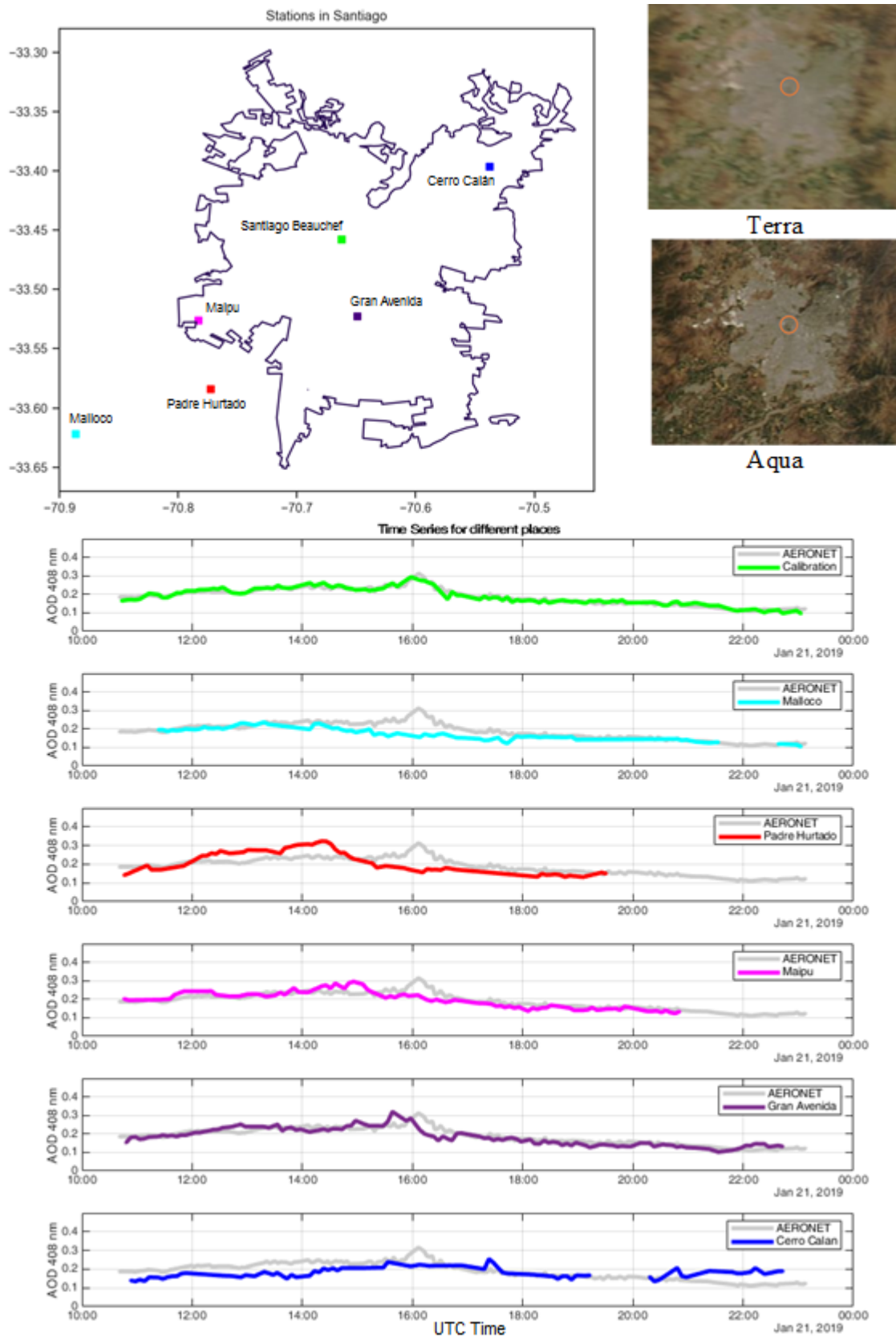Figure 5.11: City-scale measurements For January 19, 2019.

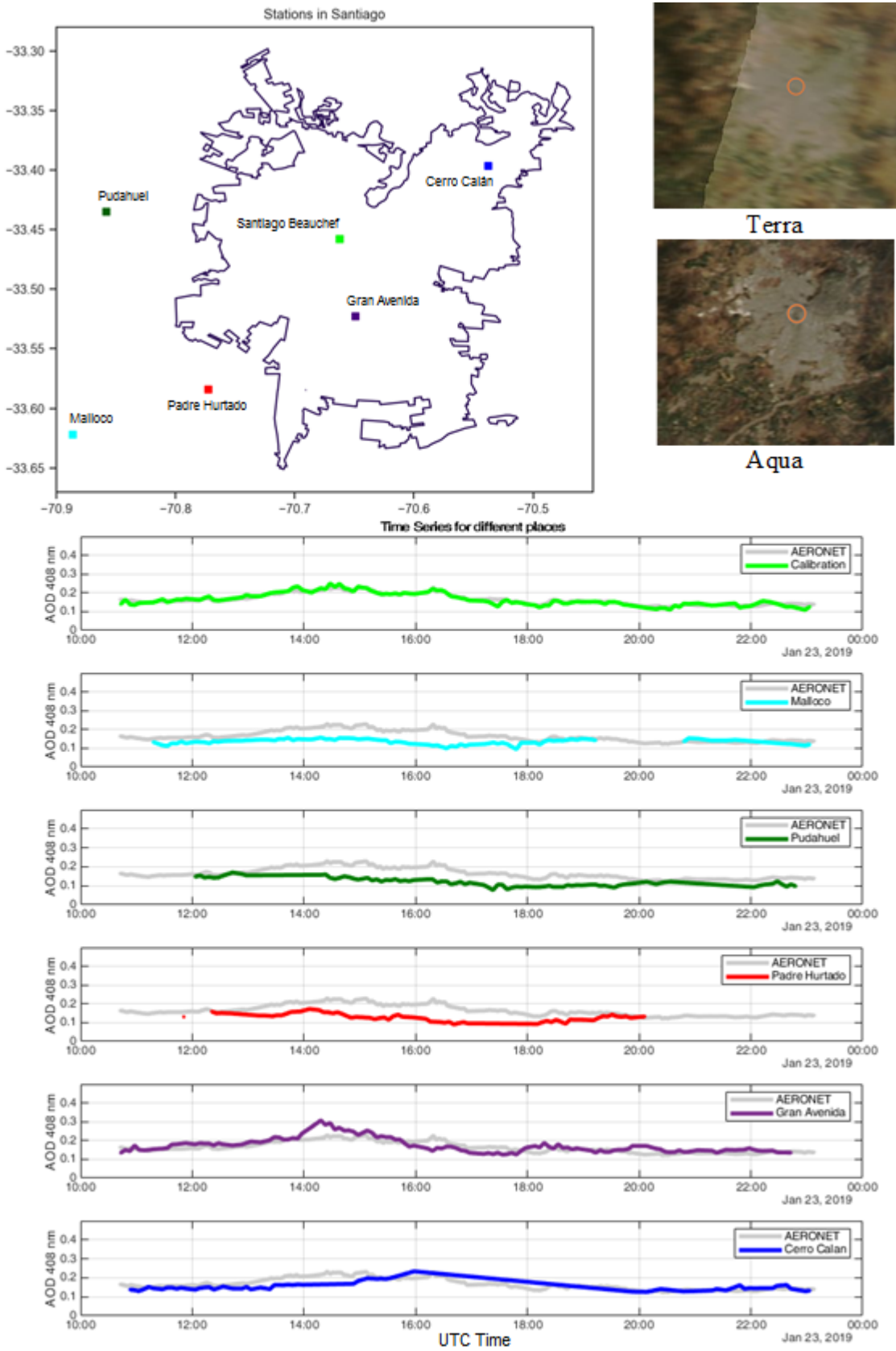Figure 5.12: City-scale measurements For January 21, 2019.

Figure 5.13: City-scale measurements For January 23, 2019.

Chapter 6

Discussion

The calibration and consistency of all the prototypes must be analyzed and discussed to determine the accuracy of the measurements performed by the instruments. In addition, an analysis of the results of the campaigns is required to identify the advantages and disadvantages of a city-scale Sun Photometer Network. Furthermore, the results need to be compared with other evidence, such as satellite images or wind model data. Finally, the main findings and future considerations have to be considered for future developments or prototypes of the network.

6.1.   Instrument's calibration and consistency.

The Langley plot calibration and the parameter fitting method proposed in this work are compared: the results of the tables 4.2 and 4.3 show a mean relative error of -1.10 % and a standard deviation of 1.16 % between the Langley constant obtained by both methods. Furthermore, the Rayleigh constant estimated by the parameter fitting method has a mean error of 0.25 % and a standard deviation of 7.84 % (In the Langley plot method, the wavelength is assumed to be known, but in the Parameter Fitting method the wavelength is considered as unknown).

These results are reasonable considering that as the first comparison. The main disadvantage of this result is it considers only punctual calibration, i.e., only calibrations obtained from one day of measurements each one is compared. For that reason and considering the approach presented by Toledano et al. (2018), the data collected with the prototype, which was measured together with the AERONET Sun Photometer for a long time (the control prototype), could be used to study the stochastic behavior of the calibration variables estimated by the Parameter Fitting method.

The control prototype measured together AERONET between January and February 2018. Figure 6.1 shows the histogram of the Langley constant and the wavelength obtained from applying daily calibration through the parameter fitting procedure explained in this document (and their conversion to log scale and Rayleigh scattering, respectively), where each bar is the frequency of parameters under the range in the x-axis. Note that there is a distribution

of the estimated variables. Therefore, Figure 6.1 indicates that to use only a day to calculate the constant could be a source of our instruments' bias due to an error in the calibration estimation. This result is not surprising because Toledano et al. (2018) present a similar approach in the case of Langley Plot calibrations [20].

The proposed Parameter Fitting estimation method considers that the AOD equation is convex for the Langley constant and the wavelength. That means, if the Langley constant is over-estimated, then the Rayleigh scattering is also over-estimated. Therefore, in the AOD calculation, both contributions are subtracted. Thus, taking the max difference between the Langley constant and the RS max bias is obtained. The results from Figure 6.1 indicate a calibration bias under 0.02 (The estimated instrument's consistency).

The complete analysis was considering two of the four sensors of this instrument. The results are summarized in Table 6.1. This Table exhibits mean deviations for the Langley constant and Rayleigh scattering around 0.02 and 0.01, respectively, which means a max average bias around 0.01 - 0.015 just because of the calibration (a relative error between 0.12% to 0.18% respecting the value of the Langley calibration constant). Therefore, by performing a calibration considering several days, this bias could be reduced. In addition, from Table 6.1 the CV (standard deviation/mean) of the Langley constant was 1.74% for sensor 1 and 1.89% for sensor 2. Comparing these CVs with the presented in Table 3.1 for the Cimel Sun Photometer, they are comparable with the UV Channel, which is reasonable considering that our sensor is in the limit between the UV and visible bands.

	Sensor 1		Sensor 2	
Variable	Mean	Standard Deviation	Mean	Standard Deviation
V_0	3356	58.42	3164	59.859
$ln(V_0)$	8.118	0.017	8.06	0.019
λ	407.2	3.3802	408.449	3.396
$Rayleigh$	0.3313	0.0116	0.3313	0.0116

Table 6.1: Mean and standard deviation for several calibration constants.

Respect the instrument's consistency related to the repeatably of the instrument. Figures 5.3 and 5.5 exhibits a standard deviation under 0.02 for all the measures made. That means all the instruments have an error under 0.02 after calibration. Table 5.3 reveals the bias is under significant numbers (an average difference among the Cimel Sun Photometer and all the prototypes of 0.0002 and a maximal difference of 0.003). These values are under the significance level to consider a bias correction in the AOD estimation, which is one order of magnitude higher.

The V3 Sun Photometers errors are compared with the reported for Holben et al. (1998) for this range of wavelengths. Our result supports the simulations performed by Toledo et al. (2018). They proved that the AOD estimation bias is not dependent on the complete spectral response of the sensors, i.e., independently of the spectral responses of the sensor are broad or narrow, the equivalent result does not change significantly. The main difference is that gases can affect the measurements, such as ozone or water vapor [25]. Our sensors were selected, taking into account no gases effect in the response spectrum (between 350 and 450 nm). As a result, the error of the instruments is similar to Cimel for the wavelength tested.
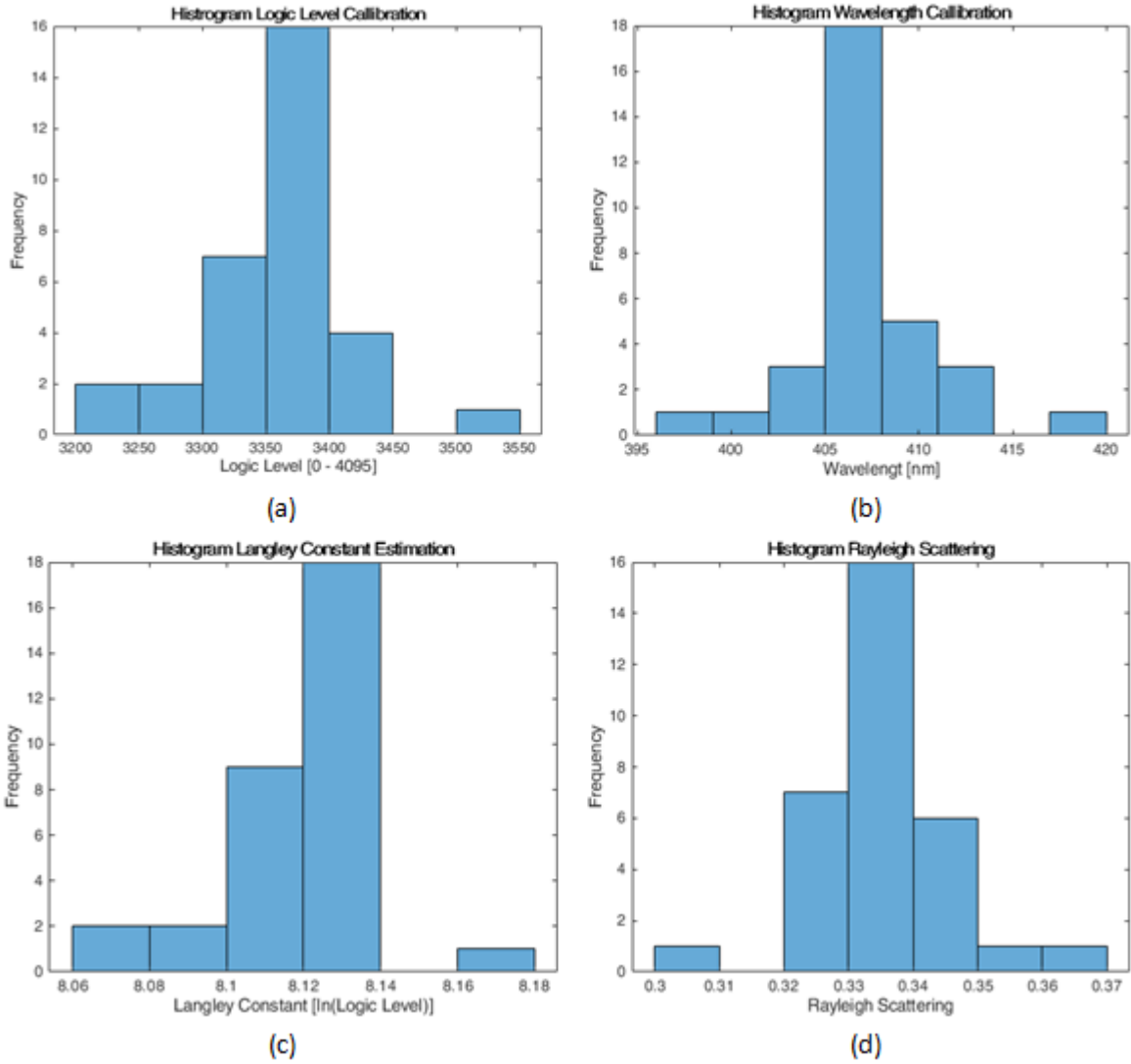
Figure 6.1: Histograms for different calibration constants. (a) Logic Level V_i. (b) Wavelength [nm]. (c) Langley constant $ln(V_i)$. Rayleigh Scattering (RS).

However, the actual Cimel error is under 0.01 after some post-process of the measurements [6].

6.2. Distributed measurement discussion.

In general, the Sun Photometer network results show a new perspective of the behavior of aerosols in the city. On one side, this spatial resolution would be impossible to achieve using Cimel Sun Photometers or geostationary satellites. On the other side, the temporal resolution would be unfeasible for LEO satellites without a constellation. Furthermore, actual LEO satellites have lower accuracy in AOD measurement for low AOD levels like Santiago measurements [5]. The mean reported error comparing with AERONET Cimel Sun Photometers considering all the measurements for satellite products is 0.12 in MODIS Collection 6 MAIAC Algorithm [7] and 0.05 for GOES-16 AOD product using an Empirical Bias Cor-

rection Algorithm [8]. Therefore, our proposed approach is an inexpensive form to increase the information about Aerosols in urban areas. That means we prove the advantages of an automated low-cost Sun Photometer network.

Taking under consideration the specific data, in some days (Figures 5.7, 5.8 and 5.9) a displacement of a large values AOD through the city is observed. This dynamic, usually from south-west to north-east in summer, is in the same direction that Schmitz (2005) displays Santiago's mean wind behavior [34]. However, in Figure 5.9, the movement is in the opposite direction. The emission of aerosols can explain this movement from a wildfire in the south-west of Santiago (red dot in the aqua satellite image in Figure 5.9). That could be studied by a denser sun photometer network, justifying the need.

A special case is exhibited on January 21th, 2018 (Figure 5.12). There was a rise of around 0.1 AOD in Padre Hurtado station. Later, this rise seems to move to the north-east. The stations of Maipu, Gran Avenida, Beauchef (AERONET), and Cerro Calan registered that move. However, Malloco station on the south-west did not register any rise. That means the rise stated between Malloco and Padre Hurtado station. Some hypotheses to explain this behavior could be an emission source or the hydration of existing aerosols in this place.

Figure 5.13 shows another interesting case. This day, the stations around the city (Malloco, Pudahuel, and Padre Hurtado) have a lower level of AOD (between 0.1 and 0.15 of AOD). In contrast, the stations inside the city have shown a different behavior during the day. It seems this day there was not emission around the city, while all the AOD dynamics occurs inside the city.

In essence, there was an observation of different AOD dynamics in the observed area when several stations were available. Only with the Sun Photometer network's spatial and temporal resolution was it possible to observe these phenomena in detail. However, there are still some challenges and improvements to the proposed sun promoter network.

6.3. Challenges and future considerations.

In this document, we explore the feasibility of an automatic low-cost sun photometer network at the city-scale. The results reveal that this network is not only attractive but also possible. It has many advantages over the usual single instrument set-up of CIMEL Sun Photometers within a city. Additionally, Toledo et al. (2018) show how to use different LED sensors and how to correct the gases effect in some bands of frequency.

Suppose we Take into consideration both works. It would be possible to develop an automatic, low-cost Sun Photometer network with different wavelength channels. However, some things need to be studied and considered before going to the next step. Examples of that are the feasibility to estimate the Ångström exponent and some instruments or logistic issues found.

6.3.1. Ångström exponent estimation error.

It is needed to estimate the Ångström exponent to determine the particle size of aerosols. However, this estimation is straightforward because of the propagation of the errors. That means, if the estimation error is too high, the exponent will be imprecise. The estimation error of the Ångström exponent is studied from two AOD values for different wavelengths.

If the Eq. 4.5 is used; it is possible to calculate the Ångström's exponent. In this case, the 380 nm and 440 nm Cimel channels estimate the AOD (because our sensors measure for a wavelength around 408 nm). Both channels have a reported error of 0.02 (assuming independent measurements), according to Holben et al. (1998). Assuming a random normal distribution of the error and then propagate the error in the equation. The result is showed in Eq. 6.1.

$$\Delta\alpha = \frac{1}{ln(\frac{\lambda_2}{\lambda_1})}(\frac{\Delta\tau_1}{\tau_1} + \frac{\Delta\tau_2}{\tau_2}) \tag{6.1}$$

In this Formula, Δ means the error of the variable. This Formula is also used by [35].

From Eq. 6.1, the error estimation depends on the absolute value of AOD for each channel. Our interest is to know how our measurements affect the Ångström exponent estimation instead of an in-depth analysis. Therefore, using the annual mean AOD values reported by Santiago Beauchef 2 CIMEL instrument and $\Delta\tau_1 = \Delta\tau_2 = 0.02$ for 380 and 440 nm channels. It is possible to have an example of the magnitude in the error of the Ångström exponent estimation.

The values obtained to the mean case ($AOD_{380nm} = 0.275$ and $AOD_{440nm} = 0.22$) shows an error estimation (standard deviation) in the Angstrom's exponent of 0.8. Typical values for this exponent value moves between 0 and 2 (The Santiago Beauchef 2 AERONET station reported a mean exponent of 1.038 during 2019, which means a relative error of 77%). Therefore, it is impossible to estimate precisely this variable for our case. On the other hand, the AOD estimation for a wavelength of 408 nm has an error of 0.027 (the Formula is not displayed here), slightly larger than the reported errors for each channel. This value is consistent with the calibration error found when comparing our instrument with AERONET CIMEL, using the Parameter Fitting method.

The Ångström exponent could be used in an inversion model to estimate the particle size distribution of the aerosols [21]. However, the Ångström exponent estimation needs to be precise. If we calculated the Ångström exponent using 440 and 870 nm, then the error for our mean case is reduced to 0.18, just a 22% of the error with two channels and reducing the relative error to 17% respecting the mean exponent.

An explanation for that is because the Ångström exponent is a slope in a log-log scale, as shows the Formula 4.4. If we use two nearest channels, the estimated slope's error will be bigger than if we use a higher wavelength. Therefore, a solution to improve the Ångström exponent estimations is using more separated wavelengths to measure AOD (considering as reference the channels chosen by Toledo et al. (2018)). A second alternative is to perform a

linear regression among different wavelength, following the AERONET procedure.

For future designs, our interest is to determine the error of this method for our mean case. Therefore, we performed a linear regression for the $N = 4$ channels of AERONET CIMEL between 440 and 870 nm (440, 500, 675, and 870 nm) using the reported errors to propagate in the Eq. 6.2, we can estimate the Ångström exponent error.

$$\Delta\alpha = \frac{\sqrt{N^2 \cdot \Sigma(|\frac{ln(\lambda_1)\Delta\tau_i}{\tau_i}|)^2 + \Sigma|\frac{\Sigma ln(\lambda_j)\Delta\tau_i}{\tau_i}|^2}}{N \cdot \Sigma ln(\lambda_i{}^2) + \Sigma|(\Sigma\frac{ln(\lambda_i\Delta\tau_i)}{\tau_i})^2|} \qquad (6.2)$$

The results show an error of 0.046 for the Ångström exponent. Consequently, if we achieve a similar error for the different channels in a prototype, it could be possible to estimate this exponent with precision and characterize the particle size of the aerosols.

From this discussion, we conclude that using we need to consider more than two channels to obtain a reasonable Ångström exponent estimation. With four-channel would be possible to have an approximate idea of the particle size distribution. The prototype presented in this work considers only one channel, although the sensor was designed to use four channels. This discussion gives an idea of the possible error estimation of the Ångström exponent using four different channels.

6.3.2.   Increasing the robustness of the instrument.

One of the biggest problems with the implementation of our Sun Photometer network was the availability of all the instruments at the same time. That occurs because the prototype has not good robustness. Some consideration and improvements to solve these issues in future instruments design to implement an extensive network of automatic sensors are:

- Check out procedure: Check all the instrument functionalities in situ to have better reliability. Instruments installed in the place without any check out routine tended to fail earlier.
- Water protection: Some instruments were installed during the rain. In most cases, the prototypes did not suffer critical damage and could measure again after a revision. However, one device was operative under extreme wet conditions and was recovered several days after the event. This instrument cannot be fixed. For this development stage, water protection was not a primary requirement because the network was only a prototype to test its feasibility. Therefore, future designs require waterproof protection, considering that it would be impossible to recover the instruments before a rain event.
- Servo motors: After a long time measuring campaign, the most usual fails of the instruments were the servomotors in the robotic arm. The servo motors are exposed the whole day on Sun. As a recommendation, it will be desired to implement a cover for the servomotors that protects them from Sun and water.
- Connection cable between the sensor and the instrument: In the beginning, a typical failure was the connection between the sensor in the robotic arm and the microcontrollers. The cable that connects the sensor to the instrument disconnected during

the operation of the prototype. In other cases, some wires cut after a few measurements. It is necessary to consider other connectors that keep the cable connected and undamaged under the robotic arm's movement.

In essence, to develop an automatic low-cost Sun Photometer with good performance is feasible considering the information obtained by this work and the work of Toledo et al. (2018) [10]. However, a dense city-scale network's success will depend on the mitigation or solution for the issues shown in this section.

Conclusion

This work's primary goal has been to evaluate the feasibility of a Low-cost and city-scale Sun Photometer network to study the variability of aerosols in urban areas: To achieve that, a prototype instrument was designed and built. Moreover, we had proposed a calibration methodology and tested the prototype iteratively to improve the prototype. Next, several improved prototype units were made, and then, the city-scale network concept was tested. The measurements of the instruments were compared with the ground truth (Cimel Sun Photometer) and with themselves.

The methodology proposed to develop the instrument was useful to achieve low-cost constraints. The final version instrument has a cost of materials of around US 220. Furthermore, the instrument is entirely unattended, and each error was improved from previous versions of the same instrument using the iterative test-improvement approach. The maximum continuous measurement for an instrument was 32 days in the Santiago Beauchef station, while the instrument which was operative for the longest time was the instrument in the Malloco station, operating for 46 days.

A different calibration procedure using the ground truth instrument as a standard was proposed. This methodology was compared with a typical Langley plot calibration. In a first approximation, the difference between the calibration parameters has a mean difference lower than 2 %. Although the Langley plot calibration could be improved by choosing a better place to perform the procedure, the ground truth instrument's calibration exhibits consistency because it can recover the equivalent wavelength of the sensors.

Comparing the errors of the developed instrument with the Cimel Sun Photometer, it was found that the average standard deviation for a day of measures is lower than 0.02 of AOD. These results are similar to the measures reported by Holben et al. (1998). In addition, the results corroborate the simulations performed by Toledo et al. (2018), whose explain that the bias and error do not depend on the spectral width of the wavelength of the sensor, only on the effects from different gases present in the atmospheres and the internal errors of the instrument. Therefore, the instrument measures are comparable with existing instruments.

After that, a distributed campaign using different stations (depending on the availability of the instruments) was performed. It was found a different behavior among the stations. The most frequent pattern was a rise of AOD in one station, and then displacement of AOD peak to near stations. Furthermore, different behavior in the dynamic of AOD was observed. These results provide evidence to show the importance of implementing a surface-based Sun Photometer network at a city-scale given that present instruments such as Cimel Sun

Photometers and Satellite estimation (an RMSE of 0.05 in the best of the cases for GOES-16 measurement [8]) or LIDARS cannot achieve either these temporal or spatial resolutions with reasonable accuracy.

In the last part, the capabilities and projection of our instruments and the network were discussed. Furthermore, we explore the possibility of determining the Ångström exponent: it was demonstrated that with the actual sensors is impossible to estimate that exponent with reasonable accuracy. Based on this, a strategy to solve this issue was established, and it could be considered to improve future designs of the instrument. After that, some problems with our prototype were identified. Finally, some ideas to solve the issues in the next generation of instruments were proposed.

In essence, a low-cost Sun Photometer sensor is feasible to implement at the city-scale. Furthermore, the prototype, the calibration methodology, and the city-scale network implementation are attractive, considering state of the art. A design and making methodology was proposed, which allows agile manufacturing and the improvement of the prototypes switching between test and modification cycles. Furthermore, this work exhibits that the error of our instrument is comparable with the ground truth instrument. Moreover, a distributed campaign was performed with the developed prototypes showing different behavior of aerosols depending on the place of measurement. Finally, some problems and challenges for future instrument improvements were found.

Bibliography

[1] J. Dayou, J. H. W. Chang, and J. Sentian, *Ground-Based Aerosol Optical Depth Measurement Using Sunphotometers.* Springer, 2014.

[2] M. D. King, D. M. Byrne, B. M. Herman, and J. A. Reagan, "Aerosol size distributions obtained by inversions of spectral optical depth measurements," *Journal of the Atmospheric Sciences*, vol. 35, no. 11, pp. 2153–2167, 1978.

[3] G. L. Schuster, O. Dubovik, and B. N. Holben, "Angstrom exponent and bimodal aerosol size distributions," *Journal of Geophysical Research: Atmospheres*, vol. 111, no. D7, 2006.

[4] B. N. Holben, T. F. Eck, I. Slutsker, D. Tanre, J. Buis, A. Setzer, E. Vermote, J. A. Reagan, Y. Kaufman, T. Nakajima, *et al.*, "Aeronet - a federated instrument network and data archive for aerosol characterization," *Remote sensing of environment*, vol. 66, no. 1, pp. 1–16, 1998.

[5] B. Liu, Y. Ma, W. Gong, M. Zhang, W. Wang, and Y. Shi, "Comparison of aod from calipso, modis, and sun photometer under different conditions over central china," *Scientific reports*, vol. 8, no. 1, p. 10066, 2018.

[6] B. N. Holben, J. Kim, I. Sano, S. Mukai, T. F. Eck, D. M. Giles, J. S. Schafer, A. Sinyuk, I. Slutsker, A. Smirnov, *et al.*, "An overview of mesoscale aerosol processes, comparisons, and validation studies from dragon networks," *Atmospheric Chemistry and Physics*, vol. 18, no. 2, pp. 655–671, 2018.

[7] A. Lyapustin, Y. Wang, S. Korkin, and D. Huang, "Modis collection 6 maiac algorithm.," *Atmospheric Measurement Techniques*, vol. 11, no. 10, 2018.

[8] H. Zhang, S. Kondragunta, I. Laszlo, and M. Zhou, "Improving goes advanced baseline imager (abi) aerosol optical depth (aod) retrievals using an empirical bias correction algorithm," *Atmospheric Measurement Techniques Discussions*, pp. 1–22, 2020.

[9] D. R. Brooks and F. M. Mims III, "Development of an inexpensive handheld led-based sun photometer for the globe program," *Journal of Geophysical Research: Atmospheres*, vol. 106, no. D5, pp. 4733–4740, 2001.

[10] F. Toledo, C. Garrido, M. Díaz, R. Rondanelli, S. Jorquera, and P. Valdivieso, "Aot re-

trieval procedure for distributed measurements with low-cost sun photometers," *Journal of Geophysical Research: Atmospheres*, vol. 123, no. 2, pp. 1113–1131, 2018.

[11] F. Volz, "Photometer mit selen-photoelement zur spektralen messung der sonnenstrahlung und zur bestimmung der wellenlängenabhängigkeit der dunsttrübung," *Archiv für Meteorologie, Geophysik und Bioklimatologie, Serie B*, vol. 10, no. 1, pp. 100–131, 1959.

[12] H. Che, G. Shi, A. Uchiyama, A. Yamazaki, H. Chen, P. Goloub, and X. Zhang, "Intercomparison between aerosol optical properties by a prede skyradiometer and cimel sunphotometer over beijing, china.," *Atmospheric Chemistry & Physics*, vol. 8, no. 12, 2008.

[13] G. S. Fargion, R. Barnes, and C. R. McClain, *In Situ Aerosol Optical Thickness Collected by the SIMBIOS Program (1997-2000): Protocols, and Data QC Analysis*, vol. 209982. National Aeornautics and Space Administration, Goddard Space Flight Center, 2001.

[14] M. J. Perri, M. R. Haggmark, D. R. Silva, and R. M. Mohs, "Inexpensive automated atmospheric measurements of aerosol optical thickness, ozone, and temperature," *Aerosol and Air Quality Research*, vol. 16, no. 2, pp. 464–469, 2016.

[15] D. Murphy, H. Telg, T. Eck, J. Rodriguez, S. Stalin, and T. Bates, "A miniature scanning sun photometer for vertical profiles and mobile platforms," *Aerosol Science and Technology*, vol. 50, no. 1, pp. 11–16, 2016.

[16] E. A. Wendt, C. W. Quinn, D. D. Miller-Lionberg, J. Tryner, C. L'Orange, B. Ford, A. P. Yalin, J. R. Pierce, S. Jathar, and J. Volckens, "A low-cost monitor for simultaneous measurement of fine particulate matter and aerosol optical depth–part 1: Specifications and testing," *Atmospheric Measurement Techniques*, vol. 12, no. 10, pp. 5431–5441, 2019.

[17] A. de Almeida Castanho, R. Prinn, V. Martins, M. Herold, C. Ichoku, and L. Molina, "Analysis of visible/swir surface reflectance ratios for aerosol retrievals from satellite in mexico city urban area," 2007.

[18] K. Boersma and J. De Vroom, "Validation of modis aerosol observations over the netherlands with globe student measurements," *Journal of Geophysical Research: Atmospheres*, vol. 111, no. D20, 2006.

[19] B. Ford, J. R. Pierce, E. Wendt, M. Long, S. Jathar, J. Mehaffy, J. Tryner, C. Quinn, L. van Zyl, C. L'Orange, *et al.*, "A low-cost monitor for measurement of fine particulate matter and aerosol optical depth–part 2: Citizen-science pilot campaign in northern colorado.," *Atmospheric Measurement Techniques*, vol. 12, no. 12, 2019.

[20] C. Toledano, R. González, D. Fuertes, E. Cuevas, T. F. Eck, S. Kazadzis, N. Kouremeti, J. Gröbner, P. Goloub, L. Blarel, *et al.*, "Assessment of sun photometer langley calibration at the high-elevation sites mauna loa and izaña," *Atmospheric Chemistry and Physics*, vol. 18, no. 19, pp. 14555–14567, 2018.

[21] O. Dubovik and M. D. King, "A flexible inversion algorithm for retrieval of aerosol optical

properties from sun and sky radiance measurements," *Journal of Geophysical Research: Atmospheres*, vol. 105, no. D16, pp. 20673–20696, 2000.

[22] J. M. Wallace and P. V. Hobbs, *Atmospheric science: an introductory survey*, vol. 92. Elsevier, 2006.

[23] J. H. Seinfeld and S. N. Pandis, *Atmospheric chemistry and physics: from air pollution to climate change.* John Wiley & Sons, 2016.

[24] Y. Cengel, *Heat and mass transfer: fundamentals and applications.* McGraw-Hill Higher Education, 2014.

[25] R. M. Goody and Y. L. Yung, *Atmospheric radiation: theoretical basis.* Oxford university press, 1995.

[26] J. E. Hansen and L. D. Travis, "Light scattering in planetary atmospheres," *Space science reviews*, vol. 16, no. 4, pp. 527–610, 1974.

[27] A. Bucholtz, "Rayleigh-scattering calculations for the terrestrial atmosphere," *Applied Optics*, vol. 34, no. 15, pp. 2765–2773, 1995.

[28] P. MacCready, "Flight on 0.33 horsepower-the gossamer condor," in *14th Annual Meeting and Technical Display*, p. 308, 1978.

[29] D. Planchard, *Engineering Design with SOLIDWORKS 2017 and Video Instruction.* Sdc Publications, 2017.

[30] M. P. Aparicio, *Diseño y desarrollo de circuitos impresos con KiCad.* Rc Libros, 2010.

[31] "Open source arduino sun tracking." `https://www.cerebralmeltdown.com/heliostatprojects/Arduino%20Sun%20Tracker%20Program/index.html`. Accessed: 2020-08-10.

[32] I. Reda and A. Andreas, "Solar position algorithm for solar radiation applications," *Solar energy*, vol. 76, no. 5, pp. 577–589, 2004.

[33] A. Ångström, "On the atmospheric transmission of sun radiation and on dust in the air," *Geografiska Annaler*, vol. 11, no. 2, pp. 156–166, 1929.

[34] R. Schmitz, "Modelling of air pollution dispersion in santiago de chile," *Atmospheric Environment*, vol. 39, no. 11, pp. 2035–2047, 2005.

[35] F. Wagner and A. Silva, "Some considerations about ångström exponent distributions," *Atmospheric Chemistry and Physics Discussions*, vol. 7, no. 4, pp. 12781–12805, 2007.